The LOFAR Transients Pipeline[☆]

John D. Swinbank[a,b], Tim D. Staley[c], Gijs J. Molenaar[b,d], Evert Rol[b], Antonia Rowlinson[e], Bart Scheers[f,b],
Hanno Spreeuw[g], Martin E. Bell[e,h], Jess W. Broderick[c,i], Dario Carbone[b], Hugh Garsden[j], Alexander J. van der Horst[b],
Casey J. Law[k], Michael Wise[l], Rene P. Breton[m,i], Yvette Cendes[b], Stéphane Corbel[j,n], Jochen Eislöffel[o], Heino Falcke[p,l],
Rob Fender[c], Jean-Mathias Grießmeier[q,n], Jason W.T. Hessels[l,b], Benjamin W. Stappers[m], Adam J. Stewart[c],
Ralph A.M.J. Wijers[b], Rudy Wijnands[b], Philippe Zarka[r]

[a]*Department of Astrophysical Sciences, Princeton University, Princeton, NJ 08544, USA*
[b]*Anton Pannekoek Institute, University of Amsterdam, Postbus 94249, 1090 GE Amsterdam, The Netherlands*
[c]*Astrophysics, Department of Physics, University of Oxford, Keble Road, Oxford OX1 3RH, UK*
[d]*Department of Physics and Electronics, Rhodes University, PO Box 94, Grahamstown, 6140 South Africa*
[e]*CSIRO Astronomy and Space Science, PO Box 76, Epping, NSW 1710, Australia*
[f]*Centrum Wiskunde & Informatica, PO Box 94079, 1090 GB Amsterdam, The Netherlands*
[g]*Netherlands Cancer Institute, Postbus 90203, 1006 BE Amsterdam, The Netherlands*
[h]*ARC Centre of Excellence for All-sky Astrophysics (CAASTRO), The University of Sydney, NSW 2006, Australia*
[i]*Department of Physics and Astronomy, University of Southampton, Southampton SO17 1BJ, UK*
[j]*Laboratoire AIM (CEA/IRFU - CNRS/INSU - Université Paris Diderot), CEA DSM/IRFU/SAp, F-91191 Gif-sur-Yvette, France*
[k]*Department of Astronomy and Radio Astronomy Lab, University of California, Berkeley, CA, USA*
[l]*ASTRON, The Netherlands Institute for Radio Astronomy, Postbus 2, 7990 AA Dwingeloo, The Netherlands*
[m]*Jodrell Bank Centre for Astrophysics, School of Physics and Astronomy, The University of Manchester, Manchester M13 9PL, UK*
[n]*Station de Radioastronomie de Nançay, Observatoire de Paris, CNRS/INSU, USR 704 - Univ. Orléans, OSUC, 18330 Nançay, France*
[o]*Thüringer Landessternwarte, Sternwarte 5, D-07778 Tautenburg, Germany*
[p]*Department of Astrophysics/IMAPP, Radboud University Nijmegen, PO Box 9010, 6500 GL Nijmegen, The Netherlands*
[q]*LPC2E - Université d'Orléans / CNRS, 45071 Orléans cedex 2, France*
[r]*LESIA, Observatoire de Paris, CNRS, UPMC, Université Paris-Diderot, 5 place Jules Janssen, 92195 Meudon, France*

Abstract

Current and future astronomical survey facilities provide a remarkably rich opportunity for transient astronomy, combining unprecedented fields of view with high sensitivity and the ability to access previously unexplored wavelength regimes. This is particularly true of LOFAR, a recently-commissioned, low-frequency radio interferometer, based in the Netherlands and with stations across Europe. The identification of and response to transients is one of LOFAR's key science goals. However, the large data volumes which LOFAR produces, combined with the scientific requirement for rapid response, make automation essential. To support this, we have developed the LOFAR Transients Pipeline, or TraP. The TraP ingests multi-frequency image data from LOFAR or other instruments and searches it for transients and variables, providing automatic alerts of significant detections and populating a lightcurve database for further analysis by astronomers. Here, we discuss the scientific goals of the TraP and how it has been designed to meet them. We describe its implementation, including both the algorithms adopted to maximize performance as well as the development methodology used to ensure it is robust and reliable, particularly in the presence of artefacts typical of radio astronomy imaging. Finally, we report on a series of tests of the pipeline carried out using simulated LOFAR observations with a known population of transients.

Keywords: astronomical transients, time domain astrophysics, techniques: image processing, methods: data analysis, astronomical databases

1. Introduction

1.1. Slow transients and variable sources

While most objects in the Universe are steady on human timescales, there are classes of sources displaying variability on timescales of years to days, seconds or fractions of a second. This variability can occur regularly, at irregular intervals, or as a singular event from a given object. Searching for these transients and variables requires observatories with a large field of view, a capability which was up to now reserved only for some optical telescopes and X- and γ-ray satellites. The radio regime is now also entering this area of time-domain astronomy, with several new facilities being built that have large fields of view (several square degrees or larger) and transients as one of their key scientific objectives (e.g., Taylor et al., 2012; Murphy et al., 2013; Tingay et al., 2013; van Haarlem et al., 2013; Bell et al.,

---

2014). A few of these observatories are probing the low radio frequency regime, from tens to hundreds of MHz, a range that has been largely unexplored so far.

Transients in the low-frequency radio sky can be divided into roughly two classes, characterized by their emission processes and the observing techniques used to study them: coherent emitters, which display very fast variability, and are found mostly in beamformed time series data, and incoherent emitters, which display slow variability and are usually detected by comparing multiple images of the same field (Fender and Bell, 2011). Here, we take the dividing line between slow and fast as ~ 1 second, which is the fastest time scale at which radio images are typically made (but see e.g. Law et al., 2011). The most well known examples of coherent emitters are pulsars and masers, but coherent emission processes are also predicted, albeit not yet discovered, for other sources like gamma-ray bursts (Usov and Katz, 2000; Sagiv and Waxman, 2002) and magnetar flares (Lyubarsky, 2014). This paper, however, focuses on searching for incoherent transients and variable sources in the image plane, on timescales from seconds to years.

The main incoherent emission process at low radio frequencies is synchrotron radiation, which arises when relativistic electrons are accelerated in strong magnetic fields. It is produced where a large amount of energy is injected into the ambient medium in jet sources and explosive events, such as X-ray binaries, active galactic nuclei, tidal disruption events, gamma-ray bursts, supernovae, magnetars, and flare stars (e.g., Dent, 1965; Gregory et al., 1972; Frail et al., 1997, 1999; Levan et al., 2011). While many of these sources show short bursts of emission at X- or γ-ray energies, their variability timescale at low radio frequencies is much longer, because the radiative lifetimes of the particles to synchrotron emission are very long, and due to synchrotron self-absorption effects (van der Laan, 1966). Although the latter decreases the sources' brightness, making their detection more challenging, it has a high pay-off scientifically since determining the evolution of the spectrum at low radio frequencies provides important information on the energetics involved in these events, the acceleration of electrons up to relativistic velocities, the generation of magnetic fields, the production and collimation of jets, and the feedback of these jets on their surroundings. Furthermore, sources with small angular scales on the sky, like active galactic nuclei, show variability which is not intrinsic but caused by scattering in the interstellar medium (Rickett, 1990). Therefore these sources are not only interesting for studying their physical properties, but can also be used to probe the medium in between them and us. In this context we note that some coherent events that are intrinsically very short can be scattered and dispersed in the interstellar medium, smearing out their signal to timescales that are probed by image transient searches (see e.g. Broderick et al., in prep.).

1.2. Detecting transients and variables

The transient sky has long been studied across the electromagnetic spectrum, but the scale of transient searches has increased markedly recently, in particular in the optical and radio regimes.

Searching for transients with large field-of-view X- and γ-ray instruments has been common for a long time, and a variety of techniques have been used for all-sky monitors on board the *Rossi X-ray Timing Explorer* (Levine et al., 1996), *Compton Gamma Ray Observatory* (Fishman, 1992), *Swift* (Gehrels et al., 2004), and *Fermi Gamma-ray Space Telescope* (Atwood et al., 2009; Meegan et al., 2009). The most common way to find rapid transients at these energies is by monitoring a large fraction of the sky, and triggering on a sudden increase in the total X- or γ-ray flux. Alternative techniques are required for transients that evolve more slowly: for instance, the Earth occultation method described by Harmon et al. (2002).

Transient searches in the image domain over similarly large fields-of-view are now planned—and, indeed, already being carried out—at optical and radio frequencies. Here, efficiently searching the extremely large data volumes produced is challenging. Optical telescopes optimized to search for transients include the Catalina Real-Time Transient Survey (Drake et al., 2009), Palomar Transient Factory (Rau et al., 2009), Pan-STARRS (Denneau et al., 2013), and the Las Cumbres Observatory Global Telescope Network (Brown et al., 2013). Several radio telescopes have dedicated transient programs as well, notably the Jansky Very Large Array (JVLA), AMI (Staley et al., 2013), MeerKAT (Karoo Array Telescope; Booth and Jonas, 2012), ATA (Allen Telescope Array; Welch et al., 2009) ASKAP (the Australian Square Kilometre Array Pathfinder; Murphy et al., 2013), the MWA (Murchison Widefield Array; Tingay et al., 2013; Bell et al., 2014), the LWA (Long Wavelength Array; Taylor et al., 2012) and LOFAR (the Low Frequency Array; van Haarlem et al., 2013). In the longer term, the Large Synoptic Survey Telescope (LSST; Ivezić et al., 2014) in the optical and Square Kilometre Array (SKA; Dewdney et al., 2010) will produce a dramatic increase in the number of transients which can be detected.

Broadly, there are two possible techniques which are adopted by these searches: difference imaging (e.g. Alard and Lupton, 1998; Law et al., 2009) or on a comparison of a list of sources measured in a given image against a deep reference catalogue (e.g. Drake et al., 2009).

Difference imaging has been demonstrated to be effective when applied to optical data, particularly in crowded fields which would suffer from source-confusion in a catalogue-based survey. However, the efficacy of difference imaging in the optical is partly due to to the sources of noise being relatively well characterised, with pixel-noise largely independently distributed and occurring on a different spatial scale to real sources (assuming a well-sampled point-spread function), and the fact that optical survey point-spread functions usually vary in a smooth fashion amenable to model-fitting.

In contrast, noise in radio-synthesis images is inherently correlated on similar scales to the sources of interest. Furthermore, effects such as radio frequency interference (RFI) and interaction between faint beam-sidelobes and bright out-of-field sources may cause artefacts which are harder to characterise and correct for than those found in optical data. As a result, higher signal-to-noise thresholds are typically applied to ensure that most spurious detections are rejected (although this process remains fallible; Frail et al., 2012). This degrades the sensitivity advantage of the difference imaging technique, and so a cataloguing survey provides equivalent results with the added benefit of recording lightcurves for individual sources.

Many recent developments, including the precursors of this work, focus on the latter approach: compiling lightcurves, storing them in a database, and then searching for transients with a variety of statistical techniques (Spreeuw, 2010; Bannister et al., 2011; Bower et al., 2011; Croft et al., 2011; Swinbank, 2011; Thyagarajan et al., 2011; Banyer et al., 2012; Hancock et al., 2012; Williams et al., 2013; Mooley et al., 2013; Bell et al., 2014). The same strategy has been adopted in this work, which describes the pipeline and methods developed for searching for transients with LOFAR. The system described here also has a broader applicability to other instruments and is developed with an eye to the long-term requirements of the SKA.

2. Transients with LOFAR

2.1. The International LOFAR Telescope

LOFAR is a recently-commissioned radio interferometer based in the Netherlands and with stations across Europe[1]. LOFAR operates in the low-frequency radio regime, observing in the frequency ranges 10–80 (low band) and 110–240 (high band) MHz, corresponding to wavelengths between 30 and 1.2 metres. The system pioneers the concept of a *software telescope*, as signals received by simple crossed-dipole antennas, which are sensitive to the whole sky, are digitized as soon as possible and signal processing is done in software. In the low band the voltages from each dipole are directly digitized; in the high band, an analogue combination of data from 16 antenna elements (a "tile") is formed prior to digitization.

In a typical imaging observation, each station acts as a phased array: the digitized data from each of the antennas in the station is coherently combined ("beamformed") to point the station in a particular direction. The field of view of beams formed in this way depends on frequency and station configuration, with the full width at half maximum ranging from 19.55° for a core Dutch LOFAR station at 30 MHz to 1.29° for an international LOFAR station at 240 MHz[2]. This beamformed data is then transported to the central processing (CEP) facility at the University of Groningen where it is correlated by a GPU-based system.

The software-based processing model provides for a great deal of flexibility. After digitization, a polyphase filter splits the data into 0.2 MHz wide subbands, the number of subbands depending on the quantization of the data: it is possible to trade off dynamic range for increased subband number and hence bandwidth: in "16 bit mode", 244 subbands are available; in "8 bit mode", 488. These subbands can be spread across frequency space, to give a large observing bandwidth (48.8 MHz in 16 bit mode). Alternatively, the beamformer can be configured to form multiple beams with different selections of subbands in different directions. In this latter mode, by trading off against observing bandwidth, an extremely wide field of view may be observed.

When operating in imaging mode, the correlator provides a dump time of 1 s, and it is this which provides a lower-limit to the timescales which can be searched for image plane transients. An alternative is to directly search high time resolution beamformed data for fast transients, as described by Stappers et al. (2011) and Coenen et al. (2014). It is also possible to configure the telescope such that beamformed and image data is recorded simultaneously, providing the greatest possible range of cadences in a transient search; ultimately, continual monitoring in this mode is an important goal.

2.2. The Transients Key Science Project and the Radio Sky Monitor

LOFAR's development and commissioning have been driven by six science areas: the epoch of reionization, deep extragalactic surveys, cosmic magnetism, solar physics and space weather, cosmic rays, and transient and variable sources. The last of these is the remit of the Transients Key Science Project[3] (TKSP; Fender et al., 2006). The TKSP's interests include transient and variable sources on all timescales, from sub-second changes in beamformed data (Stappers et al., 2011) to multi-year variability monitored through long-term imaging programmes; see van Haarlem et al. (2013) and references therein for a complete discussion of the TKSP science case. It is upon detection and monitoring in the image plane which this work concentrates.

A key programme for the TKSP is the "Radio Sky Monitor", or RSM (Fender et al., in prep.). In this mode, multiple beams from LOFAR are used to tile out a large area on the sky (Fig. 1). This field of view is then imaged on a logarithmic range of timescales, from 1 to 10000 s, and at a range of frequencies, and that image stream is searched for transient and variable sources. The survey strategy is flexible, but most plausible strategies will focus on the

---

[1] http://www.astron.nl/~heald/lofarStatusMap.html
[2] The various types of LOFAR stations together with their key parameters are listed at http://www.astron.nl/radio-observatory/

astronomers/lofar-imaging-capabilities-sensitivity/
lofar-imaging-capabilities/lofa; see van Haarlem et al. (2013) for detailed information on LOFAR's configuration.
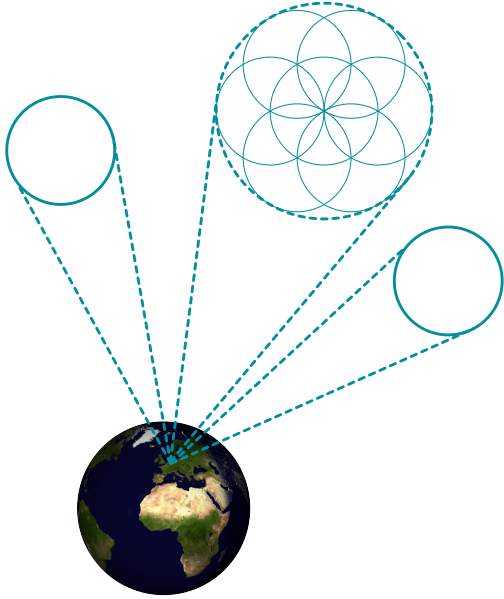[3] http://www.transientskp.org/

Figure 1: The Radio Sky Monitor concept. Multiple LO-FAR station beams tile out a large field of view, while other beams are available for target observations.

galactic plane and the zenith, while taking advantage of the large field of view to ensure that a large fraction of the sky is regularly monitored. While this procedure is ongoing, individual beams can be diverted from the ongoing survey to monitor specific targets of interest or respond to transient alerts in real time (although the latter is currently not implemented).

There are two key data products which result from this RSM: an archive of the lightcurves observed for all point sources in the LOFAR sky, and low-latency alerts of transient events. It is the TKSP's policy that, in general, these products will both be made available to the community at large.

While the RSM is running, a large volume of correlated (visibility) and image data will be generated. It is regarded as impractical to archive all of this data. Instead, an averaged version of the visibility data may be stored with reduced time and/or frequency resolution, and thumbnail images of significant detections recorded.

Ultimately, LOFAR is designed to provide low-latency "streaming" image data. When this is available, the transient search may be run, and alerts produced, in real time. At time of writing, however, this capability is still in development. Instead, visibility data is stored to disk for later "offline" imaging. This non-real-time version of the system has been deployed for LOFAR's initial operational phase. In this mode, visibility data collected by LOFAR undergoes some initial post-processing at CEP before being delivered to the TKSP. Project members then image this data on local hardware, before running the images through a version of the transients detection system which is optimized for offline use. In this way, TKSP members are able to develop our understanding of LOFAR's imaging capabilities and to test and commission the transients detection and monitoring pipeline (or "TraP") in advance of its full deployment as part of a real-time LOFAR system.

It is on this TraP system which this manuscript focuses. In §3 we provide an overview of its inputs, outputs and overall design. In §4 we describe in detail the algorithms employed by the key pipeline components, and in §5 describe the data products the pipeline delivers. Section 6 describes the pipeline implementation on a technical level. Section 7 discusses the development approaches taken. In §8 we describe testing carried out on the TraP with simulated datasets. Finally, in §10, we describe enhancements which are planned for future releases.

The TraP was developed with the aim of finding and monitoring transients in RSM-like data. However, it is worth emphasizing that it should be ultimately applicable to a much wider range of instrumentation. For example, it is planned to use the TraP to scan as much LOFAR imaging data as possible, in a so-called "piggyback" mode. An early version of the TraP has already been used in a study of archival VLA data (Bell et al., 2011), while a variant will also be deployed as the transient detection system for AARTFAAC (the Amsterdam-ASTRON Radio Transients Facility and Analysis Centre, an all-visible-sky monitor operating commensally with LOFAR; Prasad and Wijnholds, 2012). Other developments target the Arcminute Microkelvin Imager Large Array (AMI-LA; Staley et al., 2013; Anderson et al., 2014), a 15 GHz aperture synthesis aperture synthesis radio telescope near Cambridge in the UK, and KAT-7/MeerKAT, SKA-precursor telescopes in the Karoo Desert, South Africa. Further variants targeting optical data are also under consideration.

The TraP is available as open source software; for more details, refer to §10 and the code repository[4].

3. Pipeline overview

The design goal of the TraP is to automatically and rapidly identify transient and variable sources within a time-series of image data. These sources may be identified in two ways:

- *New detections* are sources which appear at a location where, in previous epochs, no source was seen;

- *Variables* are sources which have been observed for multiple epochs and show significant variability in their lightcurves.

Such sources are identified automatically by the TraP, based on no prior knowledge. It is also possible for the user to specify the location of known sources for monitoring. Variability metrics are retained for all sources, so that

---

[4] https://github.com/transientskp/tkp/

decisions on what constitutes an 'interesting source' may be made after data-processing (§5).

Since the TraP is ultimately designed to perform near real-time processing of an image stream, we assume that after an image has been processed it is no longer available for further analysis (modulo the system described in §6.5). Therefore, the TraP currently provides no capability to look back at previously processed images in the light of new data: it does not, for example, attempt to go back and check earlier images of the same position after observing a new transient. Although retaining the full image stream is unlikely to be practical for projects which generate substantial data volumes, future versions of the TraP may include the capability to generate and store an average of the input data, using this to increase the depth of the survey and improve source characterization.

3.1. Inputs

The fundamental input to the trap is a time-series of three-dimensional (two spatial, one frequency) image "cubes". These are generally assumed to be produced by the LOFAR imaging pipeline (Heald et al., 2010, 2011, 2014; van Haarlem et al., 2013), however, as described in §4.1, the code is designed to be agnostic as to the format and origin of the data being ingested.

In addition, the TraP may optionally be given a user-defined list of monitoring positions. Measurements are made and stored for each such position in each plane of every image cube ingested, regardless of whether the automatic source-finding routines regard it as significant.

3.2. Products

The TraP is designed to produce two key data products:

- Near real-time alerts to the community and/or targeted at specific partners describing ongoing transient celestial events;

- An archival database of lightcurves for all astronomical point sources detected during pipeline processing together with information about their variability.

The pipeline system is flexible enough to provide alerts in a variety of formats, and it is therefore able to interoperate with whatever mechanisms other facilities have in place for receiving notifications. For example, one can imagine e-mail or SMS being convenient. However, development has focused on the VOEvent system (Seaman et al., 2011) and its association distribution networks (Williams et al., 2012). These provide a flexible and convenient method for widespread alert dissemination, which is described in detail in §6.6.

In addition to these fundamental data products, the TraP may optionally store a copy of all the image pixel data processed for future reference. This is not required for the analysis performed by the TraP, but we have found it convenient to maintain an archive of some or all of the images processed for display purposes (e.g. using the interface described in §5.2.2).
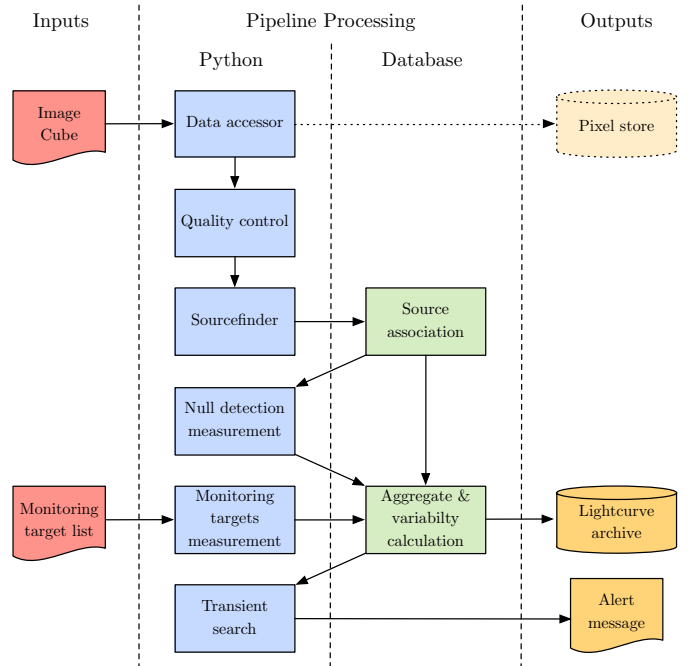

Figure 2: Transients Pipeline ("TraP") overview, showing the flow of data through the system as an image "cube" is processed, ultimately producing an archival lightcurve database and (if appropriate) transient alert messages. The individual pipeline stages are described in §3 and §4; their implementation, in terms of a mixture of Python code and database routines, is discussed in §6. The dotted parts of the diagram represent optional functionality: they are not required for the core TraP functionality.

3.3. Methods

To map from the inputs to the products described above, the following procedure is adopted. Each of these stages is described in more detail in §4; their relationship is shown graphically in Fig. 2.

1. The image cube is stored in main memory as a series of two-dimensional images, each representing a particular frequency. The in-memory representation of an image used by the TraP is independent of the on-disk data storage format; see §4.1 for details.

2. Each image undergoes a quality-control procedure, designed to identify and exclude from further processing data of unacceptably poor quality. Note that even when data is excluded by quality control it is not completely disregarded, but rather its existence and the reason for its rejection are recorded. For details of the quality control checks and the way in which they are applied see §4.2.

3. A source-finding and measurement process is applied independently to each plane of the image cube. Sources which meet the relevant significance criteria are parameterized by elliptical Gaussians. For more details on the source finding procedure see §4.3.

4. An "association" procedure is carried out, in which the new measurements are either identified as updates to the lightcurves of previously known sources, or as new, previously-undetected, sources. Details on the algorithms used for source association may be found in §4.4.

5. A list of sources which are expected to appear within the image but were *not* detected by the source finding procedure above is now constructed following the procedure described in §4.5. The same source measurement code is now used to fit and record source parameters at each of these fixed positions, and the relevant lightcurves updated accordingly.

6. The same source measurement code is used to fit and record source parameters at each of the user-specified monitoring positions, and the relevant lightcurves updated accordingly. This procedure is described in §4.6.

7. For each lightcurve in the database a series of aggregate properties describing the astronomical source are calculated. These include a weighted mean position, flux density and a series of *variability indices* which quantify the magnitude and significance of the variability of the lightcurve. This is described in §4.7.

At this point, the core loop of the pipeline is complete: the next (by time) image cube in the sequence may be ingested and the process repeats. At the same time, the results are immediately made available via a database, as described in §5.

Further analysis may be performed by querying the database for scientifically relevant phenomena and reacting appropriately. For example, one could search for all bright sources which do not have a previously-detected counterpart, and thereby identify new transients. Alternatively, a query could search for lightcurves which have reached a particular threshold in the variability indices, or which meet some other user-defined criteria.

It is important to emphasize that these queries can be performed at any time. For example, the user could wait until the complete pipeline run has been completed and archived before searching the database; equally, however, a real-time analysis system can query the database continuously as new results are added, and thereby identify new transients immediately.

As new measurements are appended to the database, continuously-updated measures such as the variability indices for a given lightcurve or the weighted mean position of the associated astronomical source will change with time. It is possible, therefore, that a particular source which was identified as variable by the real-time analysis system at some particular timestep will, in the fullness of time, be shown to not, in fact, vary significantly. In order to ensure reproducibility, the database records all the intermediate values as well as the final, archival result. That is, the user may query the archival database not just for the eventual state of a particular source, but for its state as recorded after the insertion of any particular image cube.

Finally, it should be noted that although it is possible to create LOFAR images with full polarization, and notwithstanding the ultimate TraP design goals, the current version of the TraP searches for transient and variable sources only within total intensity (Stokes I) images, and other polarization information is not used. In time, though, polarization information will be essential for properly characterizing the sources being identified: see §10 for more information on future plans.

4. Key pipeline stages

In this section we describe the logical structure of the TraP, focusing on the core stages of the pipeline and the algorithms that they employ. Section 6 describes how this logical structure is implemented in terms of deployed software and hardware resources.

4.1. Data accessors

While the TraP has been developed with LOFAR in mind, many of the core issues we are addressing are widely applicable to much of the emerging field of transient astronomy. As such, we aim to make it easy to adapt the TraP to ingest images from data sources other than LOFAR. The pipeline is designed to be data-source agnostic: the origin of the data is abstracted away from the scientific logic. This has proven to be useful as internal LOFAR data-storage standards have evolved.

Data source abstraction is achieved by defining a uniform interface which all routines in the pipeline use to access and manipulate image data. Derived classes represent data from specific sources, providing different routines for loading the data, translating telescope-specific metadata, and so on. Adding support for data from a new telescope is generally straightforward: for most instruments, just a few simple extensions to the predefined routines for working with FITS[5] or CASA[6]/`casacore`[7] are required.

This system has enabled the TraP to be used in conjunction with data not only from LOFAR but also from the VLA and AMI-LA, as described in §2.2.

4.2. Quality control

During the imaging procedure and the future real-time imaging pipeline, extremely large numbers of images will be produced for processing by the TraP. Some of these images will be of insufficient standard for transient searches: for instance, high RFI or poor calibration solutions can lead to increased noise in the image or artefacts that may be mistaken as transients.

The quality control procedure identifies and rejects those images which do not pass a range of tests. The system is modular: new tests can easily be added as required.

---

[5] http://fits.gsfc.nasa.gov/
[6] http://casa.nrao.edu/
[7] http://casacore.googlecode.com/

Further, tests may be made specific to certain instrumentation by building upon the data accessor framework (§4.1).

The standard checks supplied with the released version of the TraP are all LOFAR specific. They are:

- Test that the measured noise in the image does not significantly exceed the theoretically expected value (§4.2.1);

- Test for appropriate sampling and shape of the restoring beam parameters (§4.2.2);

- Test for proximity of the image pointing direction to bright radio sources (§4.2.3).

An image which fails one or more of these tests is not further processed. Details of the failure are logged for future reference.

These tests are designed to provide a quick and simple mitigation of common failures observed during development and commissioning. As TraP moves into production deployments, it will be possible to supplement them with a range of more elaborate tests as and when required.

4.2.1. Check for noisy images

A clear signature of a poor quality image is when the measured noise level significantly differs from the theoretically expected value: measured values which are either too low or too high are indicative of problems with the observation or its calibration.

The theoretical noise in LOFAR images can be calculated using parameters extracted from the image metadata, such as the array configuration and integration time used (Nijboer et al., 2009; van Haarlem et al., 2013).

To measure the observed RMS in an image, we conduct the following steps:

1. Select a square region congruent with the image centre and comprising 25 % of the total pixels in the image;
2. Iteratively reject pixel values more than n standard deviations from the median, where n is some user-defined parameter (typically four), until no further pixels are being rejected.
3. Using the remaining pixels, calculate the mean pixel value and the RMS scatter around this mean value.

We then calculate a simple ratio between the measured RMS noise and the theoretical noise. The image is rejected when this ratio falls outside a user-specified range.

4.2.2. Check restoring beam parameters

The properties of the restoring beam (Högbom, 1974) used to create the images used within the TraP also play a significant role in assessing the image quality. The image should be created such that the beam is appropriately sampled, with around three pixels across its minor axis. Incorrect sampling can cause increased noise, artefacts and
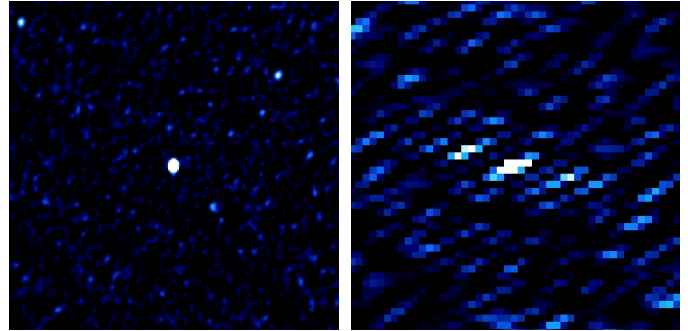
(a) Correct sampling. (b) Inappropriate sampling.

Figure 3: The effects of inappropriately sampling the restoring beam on image quality. These images are of the same field, centred on 3C 295, and they share the same physical and colour scales. At left, the image is correctly sampled, with 3 pixels across the minor axis of the restoring beam. To the right, only 1.3 pixels have been used: this image is unsuitable for pipeline processing.

spurious source detections, as illustrated in Fig. 3. The TraP aims to be robust against this, regardless of the origin of the images.

The shape of the beam is also considered. Beam shape is influenced by a variety of factors, including the array configuration, pointing direction, observing frequency and integration time. A measured shape which is significantly at variance with expectation is indicative of a failure in imaging or calibration.

TraP users can predetermine image rejection thresholds for over sampled and highly elliptical restoring beams as these may be observation or telescope dependent. All images with restoring beams which are under sampled (< 2 pixels across the FWHM) are automatically rejected by the TraP.

4.2.3. Check for proximity to bright radio sources

Poor subtraction of bright sources close to the target, during either 'demixing' (van der Tol et al., 2007) or subsequent calibration can lead to residual structures or elevated noise levels in the resultant images. Problems are typically observed close to the Sun, Jupiter and the so-called "A-Team" of bright extragalactic radio sources (de Bruyn et al., 2009): their extremely high fluxes may cause issues within target fields up to several tens of degrees away, depending on the observing configuration. To mitigate these effects, the TraP rejects images where the angular separation between the target field and a bright source is less than a user-specified threshold.

4.3. Source detection and measurement

The TraP uses a custom-developed source detection and measurement system ("sourcefinder"). The algorithms implemented are partially based on those used in SExtractor (Bertin and Arnouts, 1996), but have been extensively

re-worked and extended, most notably to provide least-squares fitting of detected sources with elliptical Gaussians and a rigorous handling of the correlated noise properties of radio images. In addition, it provides an implementation of a false detection rate algorithm (Benjamini and Hochberg, 1995; Hopkins et al., 2002).

In brief, given an input image, the system performs the following procedure:

1. Model and subtract a variable background across the image;
2. Model the RMS noise across the image;
3. Identify islands of contiguous pixels which appear above some multiple of the RMS;
4. Decompose multi-component islands into their constituent parts;
5. Perform initial estimation of source parameters;
6. Fit each component with an elliptical Gaussian and return the result.

This process results in a list of measurements describing the parameters of each source, including its position, flux density and shape as well as the significance of the detection: see Table 1 for details.

More detail on each of the sourcefinder stages is given below. For a thorough treatment, the reader is referred to Spreeuw (2010), while Carbone et al. (in prep.) presents the results of extensive testing of the sourcefinder system.

4.3.1. Background and RMS estimation

The background and noise characteristics of radio astronomy images are complex. In particular, noise across the image is correlated due to the nature of the imaging process. Since our source detection procedure relies on identifying pixels above the RMS noise, careful modelling of the background and noise maps is essential.

We start by dividing the image into a rectangular grid. The dimensions of the grid cells are user-specified; they should be chosen such that they are significantly larger than extended sources visible in the image, but fine enough to trace background variations.

We estimate the background and RMS in each grid cell through a process of iterative clipping around the median to reject source pixels. While doing this, it is important not to bias the result by rejecting source-free pixels, and to take account of the noise correlation scale.

On each iteration, we label the total number of pixels in a given cell N. We then define the number of independent pixels as $N_{\text{indep}} = N/N_{\text{dep}}$, where N_{dep} is the number of pixels per synthesized beam. We assume that source-free independent pixels follow a normal distribution, while pixels contaminated by sources do not. We therefore reject all pixels that fall more than some threshold $n\sigma$ from the median, where σ is the standard deviation of the distribution. The value of n is chosen such that we will reject, on average, one half of one normally distributed pixel. That is,

$$N_{\text{indep}} \times 2 \times (1 - F(n\sigma)) = 0.5 \qquad (1)$$

where $F(n\sigma)$ is the cumulative distribution function for the assumed normal distribution over the range $[-\infty, n\sigma]$:

$$F(n\sigma) = 0.5 + 0.5 \times \text{erf}\left(\frac{n\sigma}{\sigma\sqrt{2}}\right) \qquad (2)$$

$$= 0.5 + 0.5 \times \text{erf}\left(\frac{n}{\sqrt{2}}\right) \qquad (3)$$

$$= 0.5 + 0.5 \times \frac{2}{\sqrt{\pi}} \int_0^n e^{-t^2} \, dt. \qquad (4)$$

Inverting this, the threshold for clipping is

$$n\sigma = \sigma\sqrt{2} \times \text{erfc}^{-1}\left(\frac{1}{2N_{\text{indep}}}\right) \qquad (5)$$

where erfc^{-1} is the complementary inverse error function (Gautschi, 1972).

We estimate the sample variance based on this independent pixel count[8]. That is,

$$\sigma_{\text{meas}}^2 = \frac{N_{\text{indep}}}{N_{\text{indep}} - 1}\left(\overline{x^2} - \overline{x}^2\right) \qquad (6)$$

where σ_{meas}^2 is the measured sample variance and x represents individual pixel values. However, note that measuring the variance of a sample which has been clipped at some threshold T causes us to underestimate the variance as follows:

$$\sigma_{\text{meas}}^2 = \frac{\frac{1}{\sigma\sqrt{2\pi}} \int_{-T}^{T} x^2 \exp\left(\frac{-x^2}{2\sigma^2}\right) dx}{\frac{1}{\sigma\sqrt{2\pi}} \int_{-T}^{T} \exp\left(\frac{-x^2}{2\sigma^2}\right) dx}. \qquad (7)$$

We invert this to estimate a corrected variance

$$\sigma^2 = \sigma_{\text{meas}}^2 \frac{\sqrt{2\pi}\text{erf}\left(T/\sigma\sqrt{2}\right)}{\sqrt{2\pi}\text{erf}\left(T/\sigma\sqrt{2}\right) - 2T\exp\left(T^2/2\sigma^2\right)/\sigma} \qquad (8)$$

Note that the ratio, T/σ, of the clipping limit to the underlying standard deviation is simply the value of n which was derived following Eq. 1 in the previous iteration. Finally, following Bolch (1968), we apply a further correction to estimate the standard deviation, σ, as

$$\sigma = s \times c_4 = s \times \left(1 - \frac{1}{4N_{\text{indep}}} - \frac{7}{32N_{\text{indep}}^2}\right). \qquad (9)$$

At this point, if any pixel values are more than the calculated $n\sigma$ from the mean, they are removed from further consideration and a new iteration is started. Otherwise, the clipping process has completed.

After the pixel values have been clipped, if the field is crowded (|mean − median|/(std. dev.) ≥ 0.3) we take the

---

[8]An alternative approach would be to calculate the pixel autocorrelation function and the corresponding estimation bias correction factor (Wolter, 1984); the practical difference is minimal for plausible values of N_{indep}.

background as equal to the median; otherwise, we estimate it as

$$\text{background} = 2.5 \times \text{median} - 1.5 \times \text{mean} \quad (10)$$

following Bertin and Arnouts.

Background and RMS maps are then derived by bilinear interpolation of the background and standard deviation calculated in each grid cell.

4.3.2. Identification of significant pixel "islands"

The background map is subtracted from the input image. The noise map is multiplied by a user-specified constant ("n") to provide a threshold for finding sources. Sources are identified where the value of the background-subtracted input data is larger than the detection threshold map.

Imposing an $n\sigma$ threshold in this way implies that the fraction of pixels falsely labelled as sources in the image will be smaller than

$$\text{erfc}\left(\frac{n}{\sqrt{2}}\right) = \frac{2}{\sqrt{\pi}} \int_{n/\sqrt{2}}^{\infty} \exp\left(-t^2\right) \mathrm{d}t. \quad (11)$$

It may be more convenient, however, to quantify the number of false detections independently of the number of pixels processed. It is possible to control the false discovery rate using the algorithm described by Benjamini and Hochberg (1995). This permits the user to specify a maximum number of "false positives" (noise peaks erroneously identified as sources), and the algorithm automatically chooses an appropriate threshold for identifying sources.

4.3.3. Deblending

After the peaks of pixel islands have been identified, the islands are expanded to consist of all pixels which are contiguous with the peak pixels and which are above a further user-specified constant ("a", with $a \leq n$) times the threshold map.

These expanded pixel islands may consist of a single source, but may also include two or more sources in close proximity. We separate out the components of these composite sources in a process referred to as "deblending" (Bertin and Arnouts, 1996; Spreeuw, 2010; Hancock et al., 2012). In the deblending process, we define a number of sub-thresholds exponentially spaced between the lowest and highest pixel values in the islands. We iterate through the thresholds from lowest to highest, at each threshold checking if the island has split into two (or more) non-contiguous components, each containing a significant fraction of the integrated flux density, and each with a peak above the detection threshold $n\sigma$. If these criteria are met, we split the island and regard it as two separate sources. Both the number of sub-thresholds and the fraction of the integrated flux density required for a sub-island to be regarded as significant are user-set parameters.

4.3.4. Estimating source parameters

The peak flux density, $P_{\max}$, can be approximated by the value of the maximum pixel in the island. However, the true source peak will not coincide with the centre of the pixel. Therefore, we extend the method described by Rengelink et al. (1997), based on the assumption that the true peak lies at a random position within the pixel. This results in a correction factor of

$$\iint e^{\ln(2)\left[\frac{(x\cos(\theta)+y\sin(\theta))^2}{m^2} + \frac{(y\cos(\theta)-x\sin(\theta))^2}{M^2}\right]}\mathrm{d}x\mathrm{d}y \quad (12)$$

where M, m and θ are respectively the major and minor axes and the position angle of the synthesized beam and the integral runs over the pixel. This correction factor is multiplied by $P_{\max}$ to produce the output peak flux density.

The total flux density, F, is simply the sum of the pixel values

$$F = \sum_{i \in S} I_i, \quad (13)$$

where I_i is the value of the pixel at position x_i, y_i and $i \in S$ indicates all the pixels in a particular island.

The position of the centre of the island is given in pixel coordinates as:

$$\overline{x}, \overline{y} = \frac{\sum_{i \in S} I_i x_i}{\sum_{i \in S} I_i}, \frac{\sum_{i \in S} I_i y_i}{\sum_{i \in S} I_i}. \quad (14)$$

The position angle of the semi-major axis, measured counter-clockwise from the y-axis, is given by

$$\tan(2\theta) = \frac{2\overline{xy}}{\overline{x^2} - \overline{y^2}}. \quad (15)$$

The semi-major (M) and semi-minor (m) axis lengths are initially estimated as

$$\left\{\begin{matrix} M^2 \\ m^2 \end{matrix}\right\} = \frac{\overline{x^2} + \overline{y^2}}{2} \left\{\begin{matrix} + \\ - \end{matrix}\right\} \sqrt{\left(\frac{\overline{x^2} - \overline{y^2}}{2}\right)^2 + \overline{xy}^2}. \quad (16)$$

These axis lengths are underestimated due to the $a\sigma$ cut at the edge of the island. They are corrected by multiplying by a factor $(1 + \ln(T/P_{\max})/(P_{\max}/T - 1))^{-0.5}$, where T is the value of the RMS map times the analysis threshold a at the pixel position of $P_{\max}$.

4.3.5. Gaussian fitting

An elliptical Gaussian is fitted to each island by minimizing the error function using a modified Levenberg-Marquardt algorithm (Moré, 1977). By default, the estimated source parameters calculated above are used as initial values for fitting, and all parameters are allowed to vary. However, the user may optionally choose to hold one or more parameters to a fixed, user-specified value. Typically, this is used to constrain the fitted shape of point-like sources to that of the restoring beam.

Uncertainties on the parameters x_0, y_0 (the fitted pixel position), α, δ (the position in celestial coordinates), θ_M, θ_m

(the lengths of the major and minor fitted axes), C (the fitted peak flux density), I (the integrated flux density) and ϕ (the position angle) are calculated following Condon (1997), Condon et al. (1998) and Hopkins et al. (2003). We start by defining a generalized "signal-to-noise ratio" as

$$\rho^2 = \frac{\theta_M \theta_m}{4\theta_B \theta_b} \left[1 + \frac{\theta_B^2}{\theta_M^2}\right]^{\alpha_M} \left[1 + \frac{\theta_b^2}{\theta_m^2}\right]^{\alpha_m} \frac{C^2}{\sigma^2} \quad (17)$$

where σ is the RMS noise at the location of the source and $\alpha_M, \alpha_m = (1.5, 1.5)$ for amplitude errors, $(2.5, 0.5)$ for errors on x and θ_m and $(0.5, 2.5)$ for errors on y, θ_M and ϕ (Condon, 1997).

Given the above definitions, we apply the relationships described by Condon (1997) and Hopkins et al. (2003) to obtain

$$\frac{2}{\rho^2} = \frac{\sigma_C^2}{C^2} \quad (18)$$

$$= 8\ln 2\frac{\sigma_{y_0}^2}{\theta_M^2} = 8\ln 2\frac{\sigma_{x_0}^2}{\theta_m^2} \quad (19)$$

$$= \frac{\sigma_{\theta_M}^2}{\theta_M^2} = \frac{\sigma_{\theta_m}^2}{\theta_m^2} \quad (20)$$

$$= \frac{\sigma_\phi^2}{2} \frac{(\theta_M^2 - \theta_m^2)^2}{\theta_M^2 \theta_m^2} \quad (21)$$

$$\sigma_\alpha^2 = \sigma_{x_0}^2 \sin^2\phi + \sigma_{y_0}^2 \cos^2\phi \quad (22)$$

$$\sigma_\delta^2 = \sigma_{x_0}^2 \cos^2\phi + \sigma_{y_0}^2 \sin^2\phi. \quad (23)$$

Note that, for simplicity, the above assumes that the fitted major axis of the source aligns with the y axis of the pixel grid. If this is not the case, a further rotation is required. Finally, the integrated flux density and its variance are given by

$$I = C\frac{\theta_M \theta_m}{\theta_B \theta_b} \quad (24)$$

$$\frac{\sigma_I^2}{I^2} = \frac{\sigma_C^2}{C^2} + \frac{\theta_B \theta_b}{\theta_M \theta_m} \left[\frac{\sigma_{\theta_M}^2}{\theta_M^2} + \frac{\sigma_{\theta_m}^2}{\theta_m^2}\right]. \quad (25)$$

After fitting, the Gaussian restoring beam is deconvolved from the resultant source parameters using an algorithm derived from that provided by AIPS (Greisen, 2003), so that the deconvolved shape parameters ϑ_M, ϑ_m and φ are given by

$$\beta^2 = (\theta_M^2 - \theta_m^2) + (\theta_B^2 - \theta_b^2) \quad (26)$$

$$- 2(\theta_M^2 = \theta_m^2)(\theta_B^2 - \theta_b^2)\cos 2(\phi - \Phi) \quad (27)$$

$$2\vartheta_M^2 = (\theta_M^2 + \theta_m^2) - (\theta_B^2 + \theta_b^2) + \beta \quad (28)$$

$$2\vartheta_m^2 = (\theta_M^2 + \theta_m^2) - (\theta_B^2 + \theta_b^2) - \beta \quad (29)$$

$$\varphi = \frac{1}{2}\mathrm{atan}\frac{(\theta_M^2 - \theta_m^2)\sin 2(\phi - \Phi)}{(\theta_M^2 - \theta_m^2)\cos 2(\phi - \Phi) - (\theta_B^2 - \theta_b^2)} + \Phi. \quad (30)$$

Following this procedure, the parameters described in Table 1 are returned by the sourcefinder and are ready for insertion into the pipeline database.

Name	Units	Notes
Right ascension (α)	J2000 deg.	
Declination (δ)	J2000 deg.	
Peak flux density	Jy/beam	
Integrated flux density	Jy	
Significance	-	Peak/RMS
Lengths of semi-axes	arcsec	
Position angle	deg.	North through east
Error radius	arcsec	Absolute error on source centroid

Table 1: Parameters returned by the sourcefinder routines.

4.4. Source association

Each individual astronomical source detected in a given set of images is assigned a unique identification in the form of an entry in the "running catalogue". The running catalogue ties together a series of measurements made in individual images with aggregated information about the source derived from those measurements (its position, variability information, etc; see §4.7). The complete set of measurements associated with a particular running catalogue entry comprise its lightcurve.

4.4.1. Association procedure

The association procedure adopted is based on de Ruiter et al. (1977), Sutherland and Saunders (1992) and Rutledge et al. (2000), and is described in detail in Scheers (2011). For each measurement, the source association procedure searches for counterparts in the running catalogue. The algorithm relies on the de Ruiter radius, the angular distance on the sky between source i and its potential association counterpart j normalized by the positional error of both sources. The de Ruiter radius is defined as

$$r_{i,j} = \sqrt{\frac{(\alpha_i - \alpha_j)^2 \cos^2((\delta_i + \delta_j)/2)}{\sigma_{\alpha_i}^2 + \sigma_{\alpha_j}^2} + \frac{(\delta_i - \delta_j)^2}{\sigma_{\delta_i}^2 + \sigma_{\delta_j}^2}} \quad (31)$$

where α_n is the right ascension of source n, δ_n is its declination, and σ_q represents the error on the quantity q.

If sources i and j are genuinely associated, their positional differences will be due to measurement errors, and hence follow a Rayleigh distribution (e.g. de Ruiter et al., 1977). The probability of source association at $r \geq \rho$ is then

$$p_r(r \geq \rho) = \int_{r=\rho}^{\infty} r\exp(-r^2/2)\mathrm{d}r = \exp(-\rho^2/2). \quad (32)$$

This may be used for determining the search radius, r_s, of the area that will be scanned for possible counterparts: a search radius of $r_s \leq 3.71$, will miss a factor of 10^{-3} of the possible association counterparts, while $r_s \leq 5.68$ will miss a factor of 10^{-7}.

Given the above definition, the source association procedure regards a particular measurement as being associated

with a given running catalogue source if their positions are no further apart than the semi-major axis of the restoring beam and the de Ruiter radius is less than a user-specified threshold. Note that the calculations above only consider repeat measurements of a single, isolated source. If the TraP is to be used in processing observations of crowded or extremely transient-rich fields of view, this will require further consideration of the trade-off in search radius between missed self-associations, and spurious associations between distinct sources. Making an optimal choice of search radius for a crowded field will depend on the precise spatial clustering of sources, an issue which is not investigated further here.

4.4.2. Association types

The procedure described above does not guarantee a unique association between each source measurement and a single running catalogue source. Instead, there are various possible association topologies, as illustrated in Fig. 4 and discussed below.

Note that the association is based upon the positions and associated uncertainties of a particular measurement and the equivalent aggregated quantities for running catalogue sources; no reference is made to time or frequency in assessing whether a particular pair is associated. The discussion below refers to "time", but the same considerations apply to association along a frequency axis. This has the consequence that the order in which data is associated affects the result, and hence the reproducibility of a particular analysis. This is discussed in more detail in §4.7.3.

No association. The source measurement cannot be associated with any previously catalogued sources. We regard this as a newly detected source, and create a catalogue entry for it.

One-to-one. The flux density measurement is unambiguously associated with a single running catalogue entry, as shown in Fig. 4a. The average flux density of the source L_1 is $\overline{f_{1\ldots4}}$.

Many-to-one. Many-to-one associations exist when two or more running catalogue sources satisfy the association criteria for a given measurement. We record this in the database as multiple separate one-to-one associations. This is illustrated in Fig. 4b: at times t_1 and t_2 distinct lightcurves, L_1 and L_2 are being tracked. However, at t_3 a single source is detected which can be associated with both of these lightcurves. This could happen, for example, if the third observation was made at a lower angular resolution.

Note that the single flux density measurements f_5 and f_6 are now independently included in two separate sources: L_1 has average flux density $\overline{f_{1,3,5,6}}$ and L_2 has average flux density $\overline{f_{2,4,5,6}}$. The total brightness reached by summing all catalogued source flux densities has been artificially increased. Since all individual measurements are stored,
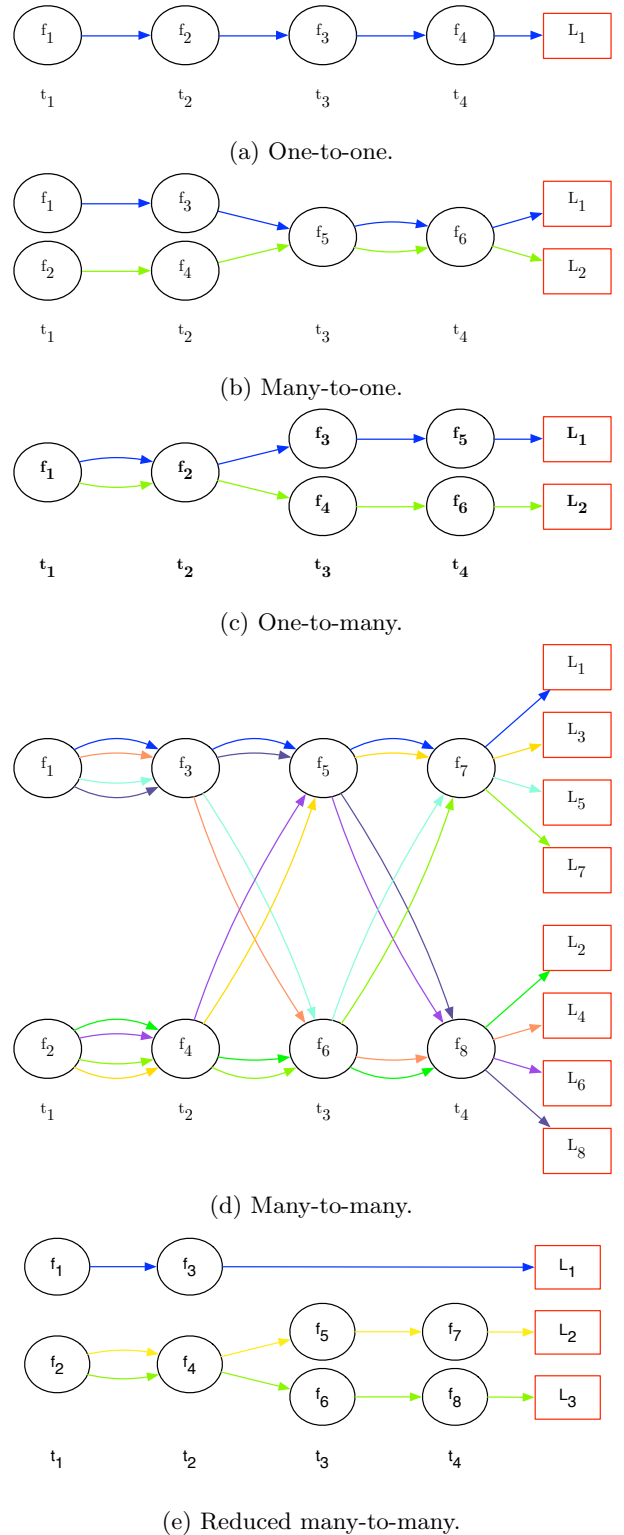

(a) One-to-one.

(b) Many-to-one.

(c) One-to-many.

(d) Many-to-many.

(e) Reduced many-to-many.

Figure 4: Types of source association, corresponding to those described in §4.4.2. Flux density measurements taken at a particular position at time t_a are labelled f_b. The association procedure knits flux density measurements together between timesteps to form lightcurves which are identified with particular running catalogue entries identified as L_c.

it is possible for users to correct for this in their analysis according to their particular requirements. Future versions of the TraP may support the division of flux density from a single measurement among multiple sources (§10).

One-to-many. In the reverse of the previous case, a single running catalogue source can be associated with more than one source measurement from a given image. This is handled by splitting the catalogue source into two independent sources, L_1 with average flux density $\overline{f_{1,2,3,5}}$ and L_2 with average flux density $\overline{f_{1,2,4,6}}$ as shown in Fig. 4c. As in the many-to-one case, some source measurements are included in multiple lightcurves, artificially increasing the total brightness of the catalogue.

Many-to-many. A many-to-many association occurs when more than one running catalogue source can be associated with more than one extracted source. If the procedures described above were applied, every possible combination of catalogue sources and new measurements would result in a new lightcurve: the database complexity would increase quadratically, and the situation rapidly becomes untenable. This is illustrated in Fig. 4d. To prevent this, many-to-many associations are reduced to one-to-one or one-to-many associations by choosing only the source pairs with the smallest de Ruiter radii. By applying this procedure, the association topology is reduced to a simpler case such as that shown in Fig. 4e: rather than the eight separate lightcurves produced by "pure" many-to-many association, we are left with just three.

4.5. Null-detection handling

We use the term "null-detection" to describe a source which was expected to be observed in some particular image—it had been observed in previous images of the same field with a flux density above our detection threshold for this image—but which was not detected by the source finding procedure (§4.3).

After the association step (§4.4), we build a list of all sources which:

- Exist in the list running catalogue of known sources, having been observed (in any frequency band) at an earlier timestep;

- Were not associated with any source detected in the current image.

For each of these null detections, we use a modification of the sourcefinding procedure: the same techniques are employed for background and noise estimation and source measurement as previously described, but, rather than being based on islands of pixels above some threshold, the peak of measurement is constrained to be fixed to the catalogued position of the null detection. No other additional constraints are placed on the measurement.

After the measurement has been made, it is stored as a one-to-one association with the appropriate running catalogue entry; the measurement is marked as being due to the null detection procedure.

In the current release of the TraP, once a running catalogue entry has been created, forced fitting at that location will always be attempted in the absence of a matched blind-detection. Ultimately, an accumulation of marginal single-epoch false detections due to noise will cause a very large number of irrelevant forced fits to be performed and stored. This may be mitigated by expiring these marginal detections from the list of positions to be measured if they are not re-observed after a certain period of time or number of revisits. Automatic expiry according to user-defined criteria will be included in a later release of TraP.

4.6. Monitoring list sources

We anticipate that there may be some sources which are important to particular science cases which may not always be detected by the default sourcefinding procedures employed by the TraP. It is therefore possible for the end-user to supply a "monitoring list" of positions at which a measurement will always be made, regardless of the results of the sourcefinding step. The current version of the TraP assumes that input images have been correctly registered when making these measurements: it makes no attempt to correct for astrometric shift.

For each image which covers the location of a position on the monitoring list, a measurement is taken at its location. The same procedure is used as for null detections (§4.5): a modified version of the algorithms described in §4.3 which hold the position of the measurement constant.

For each monitored position, a running catalogue source is generated which contains only a chain of one-to-one associations of measurements at the user-specified position. Sources monitored in this way are not included in the general association procedure described in §4.4.1.

4.7. Aggregate source properties

For each entry in the running catalogue, we now have at least one individual measurement (corresponding to the current image) and potentially others corresponding to other images (presumably representing observations at different times or frequencies). We combine these measurements to estimate the true source properties as follows.

4.7.1. Mean values

For each property of a given source we store both the arithmetic mean and a weighted mean. For a series of measurements of property x, we denote the arithmetic mean of x as $\overline{x}$. We define the weight of a measurement of property x as

$$w_x = 1/\sigma_x^2 \tag{33}$$

where σ_x is the uncertainty on that measurement. The weighted mean of N such measurements is then

$$\xi_x = \frac{\sum_{i=1}^{N} w_{x_i} x_i}{\sum_{i=1}^{N} w_{x_i}}. \tag{34}$$

Using these definitions, for each source we calculate both the arithmetic and weighted means of:

- The source right ascension (J2000 degrees);

- The source declination (J2000 degrees).

For each frequency band for each source, we calculate both the arithmetic and weighted means of:

- The peak flux density of the source in this band (Jy/beam);

- The integrated flux density of the source in this band (Jy).

4.7.2. Variability metrics

After source association, each running catalogue entry corresponds to a multi-frequency lightcurve of a particular source. We search for transient and variable sources by examining the properties of these lightcurves.

For each source, we label a measurement of its flux density at a particular frequency, ν, as I_ν with uncertainty σ_ν. Based on these quantities, and using the same notation as above, we define the flux density coefficient of variation[9] over N measurements as the ratio of the mean flux density to the sample standard deviation s, thus:

$$V_\nu = \frac{s}{\overline{I_\nu}} = \frac{1}{\overline{I_\nu}} \sqrt{\frac{N}{N-1} \left(\overline{I_\nu^2} - \overline{I_\nu}^2 \right)}. \qquad (35)$$

Using the same definition of weight $w_\nu = 1/\sigma_\nu^2$ as above, we can also express the significance of the flux density variability. We make use of the familiar reduced-χ^2 expression in conjunction with the weighted mean flux density, ξ_{I_ν}:

$$\eta_\nu = \frac{1}{N-1} \sum_{i=1}^{N} \frac{(I_{\nu,i} - \xi_{I_\nu})^2}{\sigma_{\nu,i}^2}. \qquad (36)$$

For a given η_ν, the probability that we can reject the null hypothesis—that the source under consideration is not variable—is given by

$$P_{\text{variable}} = 1 - \int_{\eta_\nu' = \eta_\nu}^{\infty} p\left(\eta_\nu', N-1\right) d\eta_\nu'. \qquad (37)$$

where $p(x, n)$ is the χ^2 probability density function for x over n degrees of freedom (see, for example, Kesteven et al., 1977).

V_ν and η_ν are calculated and stored for every lightcurve whenever a new source measurement is added. Since variability metrics are stored per association, we can track how

the variability parameters of a source have changed with time. This is particularly useful in the case of those sources which have shown evolution in their behaviour over time.

It is worth noting that it would be relatively straightforward to extend the TraP to support the calculation and storage of other variability metrics beyond the two described above. It is expected that extended testing and experience in processing data from various sources will guide future development in this area.

4.7.3. Reproducibility of results

Reproducibility of pipeline results is of paramount importance: the end user should be confident that repeatedly running the TraP on a given dataset with the same configuration should always produce the same results. This has important consequences for the association and aggregation procedures. For example, consider a particular running catalogue source R and two source measurements, M_1 and M_2, taken from different images. If M_1 is inserted first, it is associated with R. On association, a new aggregate position for R is calculated (which may or may not be consistent with association with M_2). On the other hand, if M_2 is inserted first, the resulting aggregate position for R is *not* consistent with association with M_1. In short, the order in which the images are processed influences the association procedure, and hence changes the outputs.

In order to mitigate this effect, the TraP only guarantees reproducibility of output if the input is in monotonically increasing order of time. If two or more images with different frequency or Stokes parameters but the same timestamp are processed, the TraP will automatically sort them along these axes before processing. This is not, in general, possible along the time axis, which is potentially unbounded.

5. Data products

After all the stages described in §4 have been completed for a given image cube, the core pipeline loop is complete. The complete running catalogue, together with ancillary data describing the images which have been processed, pipeline configuration and other metadata, is now stored in a database, the structure of which is described in detail in §6.4. At this point, the pipeline may start processing the next image cube. Simultaneously, the contents of that database may be used to support scientific analysis and alert generation.

5.1. Identifying transient events

As described in §3, we distinguish between newly detected and variable sources. Both are scientifically significant and may form the basis for a "new transient" alert. Depending on context and science goal, these alerts may simply result in a particular source being brought to the attention of the pipeline end user, or they may be distributed more widely to the community. The technical mechanism used for alert dissemination is described in §6.6.

---

[9]This quantity is occasionally referred to as the 'modulation index' in astronomical literature (e.g. Narayan, 1992; Gaensler and Hunstead, 2000; Jenet and Gil, 2003; Bell et al., 2014). The present authors prefer 'coefficient of variation' due to its more widespread use (McKay, 1932; Hendricks and Robey, 1936; Lande, 1977; Freund and Williams, 2010) and because it avoids any possible confusion with other fields (e.g. Whitaker, 1996).

5.1.1. New detections

As described in §4.4.2, a measurement which cannot be associated with a previously catalogued source is regarded as a new detection. Such a new detection might correspond to a new transient source appearing, but it could also simply mean that this area of sky had not previously been surveyed to a depth adequate to detect this source.

In order to distinguish between these possibilities, the TraP keeps track of the fields-of-view and sensitivities of all images it processes. When a new source is detected, its flux density is compared against the recorded sensitivities of images covering the same area to see if it could have been detected previously. If so, it may be regarded as a new transient.

In practice, and as described in §4.3.1, noise (and hence sensitivity) is not constant across any given image. It is possible that a particular source could have been detected if it fell in a low-noise area of a previous image, but not if it fell in a high-noise area. We therefore record both the highest and lowest RMS values recorded in each previous image ($\sigma_{\max,i,\nu}$ and $\sigma_{\min,i,\nu}$ in image i at frequency ν) as well as the detection threshold ($n_{i,\nu}$) used when processing that image. For a flux density measurement $I_{i,\nu}$, we regard it as a marginal transient candidate if

$$\sigma_{\max,j,\nu} \times (n_{j,\nu} + M) > I_{i,\nu} \geq \sigma_{\min,j,\nu} \times (n_{j,\nu} + M). \quad (38)$$

where M is some user specified margin, applied to prevent stable sources with flux densities approximately equal to the detection threshold from being misidentified as transients. This marginal category would include both genuine but faint transients, and steady state sources which change in significance as noise varies between images. In the case that

$$I_{i,\nu} \geq \sigma_{\max,j,\nu} \times (n_{j,\nu} + M) \quad \forall j < i \quad (39)$$

we regard the source as likely to be a new transient.

5.1.2. Variable sources

As per §4.7.2, three separate variability metrics—the flux density coefficient of variation V_ν, the significance of the variability η_ν, and the probability of variability P_{variable}—are stored whenever a new source association is made. We can therefore search the catalogue for sources which meet the following criteria:

- V_ν is above a user-specified threshold;

- η_ν is above a user-specified threshold;

- P_{variable} is above a user-specified threshold;

- The number of source measurements in the lightcurve is above a user-specified threshold.

Choosing appropriate values for these thresholds is a matter of user configuration and will depend on the details of the science case as well as the particular dataset under investigation. Section 8 gives an overview of possible considerations, while Rowlinson et al. (in prep.) presents a detailed consideration of how optimal parameters might be chosen.

5.2. Database interface

While automatic routines may be used to scan the database for transients as it is constructed using the methods described in §5.1, it is likely that many scientific discoveries will be based on expert analysis of the database contents. Here, we describe the systems by which this is made available to end users.

5.2.1. Direct database queries

The core database engine is one of various off-the-shelf database management systems, as discussed in detail in §6.4. Given appropriate permissions[10], the database may be queried directly using SQL[11]. Expert users may write SQL scripts or use the command line interface to the database system to manually construct complex queries selecting exactly the information they require.

5.2.2. Web interface

While the ability to query the database for arbitrary information which answers a specific science question is undeniably powerful, it requires a significant investment of time on the part of the end user to become fluent in the relevant technologies. Further, it is often convenient to have an at-a-glance summary of the contents of the database and the important results. For this reason, the TKSP has developed *Banana*, a web-based interface to the database. Banana enables the user to conveniently examine the contents of the database, viewing details (including cutout images) of all source measurements, plotting lightcurves of all sources in the running catalogue, selecting potential transients based on their variability metrics, and so on.

Banana is open-source (it is released under a Modified BSD license[12]) and is developed and released by the TKSP independently of the TraP. It is freely available for download[13].

5.2.3. High volume archival data-mining

For modest input dataset sizes (thousands of images, tens or hundreds of sources per image), the total volume of data stored is modest: on the order of, perhaps, gigabytes. However, as per §2.2, the TraP ultimately aims to support long term operation of the LOFAR RSM, which will be capable of producing thousands of images per hour. It is also a stated aim of the project to make the lightcurve

---

[10]Database permissions are controlled by the administrators of a particular TraP installation; it is possible for them to grant permissions to both query and modify the data to arbitrary users if required.

[11]Structured Query Language, the de-facto standard for interacting with relational database systems.

[12]http://opensource.org/licenses/BSD-3-Clause

[13]https://github.com/transientskp/banana

archive available to the community as a legacy resource. Efforts are currently underway to both develop database systems capable of handling this volume of data (Scheers, 2011; Scheers et al., in prep.), and a batch query system akin, for example, to CasJobs (O'Mullane et al., 2005) is under consideration. Ultimately, we also hope to make data available using a Virtual Observatory-compliant interface. However, the currently-available IVOA model for time series data (Graham et al., 2014) is an intentionally minimal interim solution; we prefer to wait for more mature standards to become available (e.g. McDowell et al., 2015) before proceeding.

6. Implementation

In this section, we turn our attention to the underlying technology which implements the workflow described in sections 3 and 4.

6.1. Architecture

The TraP is structured as a series of pipeline "steps", each of which performs a logically discrete operation in turn. These steps, and the relationship between them, are shown graphically in Fig. 2.

The operations carried out by the TraP naturally split into those which involve directly interacting with image data (such as loading data from disk or finding and measuring sources within it) and those which operate on measurements derived from the data (source association or aggregate calculation).

Interacting with images and performing measurements upon them is most effectively accomplished by bespoke software packages developed by members of the TKSP which directly encode the required algorithms. We have developed a series of such packages using the Python programming language[14]. The choice of Python for this task, together with a discussion of the approach taken, is motivated in §6.2.

The derived data which results from source measurements is highly structured. It can be efficiently stored using a relational database system (Codd, 1970). The contribution of the database goes beyond mere storage, however: by performing calculations within the database itself it possible to operate on the entire corpus of data efficiently and with minimal overhead due to data transport. In this way, the database becomes the core computational engine of the TraP. The design and structure of the database is described in §6.4.

A control layer sits above the core scientific logic as defined in Python code and the database. This control layer defines the structure of the pipeline—effectively connecting the components together in the correct order—as well as providing utility services such as parallelization and task distribution, which we describe in §6.3.

Finally, and in addition to the pipeline routines described, the TraP offers the option to save a copy of all the pixel data processed to a separate document-oriented database for later use by the Banana web interface (§5.2.2). This is described in §6.5.

6.2. Python

Python is the primary programming language used in the TraP. We consider Python to be the default choice for astronomical software development where performance is not the critical consideration in the near to intermediate future. It provides a flexible and expressive language together with a wide ecosystem of scientific and other libraries, and it is easily extensible using code written in lower-level languages where maximum performance is required[15]. Furthermore, thanks to projects like IPython (Pérez and Granger, 2007) and AstroPy (Astropy Collaboration et al., 2013), Python is also increasingly finding a role in the daily workflow of many astronomers as an interactive data analysis toolbox. Although we do not directly use these tools in the TraP, this familiarity then lowers the barrier to entry on larger projects as the novice coder becomes more proficient, potentially widening the pool of future maintainers and contributors to open-sourced scientific codes.

Although we have had great success using Python, a significant downside is that, as a dynamically typed language, there is a risk of run-time type errors. We have countered this by adopting a strongly test-focused development style and building an extensive suite of TraP unit tests. This is a topic we return to in §7.4.

6.3. Parallelization and distribution

Some operations which are carried out by the TraP can be performed concurrently on multiple datasets. For example, the initial source finding and measurement step (§4.3) can be performed on many independent images simultaneously without changing its results. We can exploit this intrinsic parallelism to obtain the best possible run-time performance by distributing processing across multiple CPU cores (or even distinct machines) and scheduling as many operations to run concurrently as is possible.

Of course, the performance improvement which may be achieved in this way is limited: some operations (such as source association, §4.4) cannot run concurrently (we rely on data being processed in a particular order to ensure reproducibility; §4.7.3); there is an intrinsic ordering of pipeline steps (it is impossible to perform source association before source measurement is complete); and, for reasons of reproducibility, we mandate that all steps relating to images corresponding to a particular observation time are complete before a subsequent observation time can start

---

[14]http://www.python.org/

[15]We have experimented with writing portions of the TraP in Cython (http://www.cython.org/) for performance reasons with some success, but no Cython code is shipped with the current release.

processing (§4.7.3). These intrinsically sequential parts of the processing limit its overall performance (Amdahl, 1967).

We have implemented the TraP in such a way that the definition of the underlying algorithms is independent of the method used to start tasks and collect results. In this way, it is possible to insert different task scheduling back-ends which support different parallelization and distribution techniques. Three are currently supported by the TraP:

- The *serial* back-end runs tasks sequentially using a single Python interpreter. Using the standard Python interpreter[16] means that all (non-database) processing takes place in series on a single CPU core.

- The *multiproc* back-end uses the `multiprocessing` package[17] to schedule jobs on multiple CPUs within a single machine concurrently.

- The *celery* back end uses Celery[18], an asynchronous task distribution system, to marshal the distribution of concurrent TraP tasks across a cluster of multiple machines.

The end user may select which back-end to use when invoking the TraP from the command line.

Note that the `celery` system does not arrange for data to be transmitted across the cluster. If, for example, it is used to distribute a source finding step across multiple images, it is required that each machine have access to the particular images which it is to process (perhaps on its local disk or on shared storage). This is a convenient match to the imaging process on the LOFAR cluster, which deposits image data on the cluster node which was responsible for creating it. We have, nevertheless, prototyped an image transmission system which is better integrated with the TraP, but it is not included in the current release.

Many-core exploitation works well for the 'embarrassingly parallel' problem of sourcefinding across many different images (corresponding to different frequencies and pointings). However, the bottleneck for processing a timestep then becomes the database operations, placing stringent performance requirements on the combination of query complexity and database back-end used, as covered in Section 6.4.

6.4. Database

All source measurements, together with metadata describing the images from which they were taken, are stored and processed in a relational database. The contents of the database is itself one of the core products of the TraP (§3.2), while queries run over the database are an intrinsic part of regular pipeline processing. Only a single instance of the TraP may write to a given database during processing (but the database may be accessed by arbitrary read-only queries). However, both of the supported database management systems, as described in §6.4.1, provide for multiple isolated databases being hosted within a single system, so supporting multiple pipeline instances is straightforward. This could be used, for example, to support multiple independent monitoring campaigns.

6.4.1. Database management systems

The TraP is developed and tested using two relational database management systems (RDBMS): MonetDB[19] and PostgreSQL[20].

MonetDB is an ongoing project to build a database with exceptional performance and scalability based on research into data organization and query optimization (Idreos et al., 2012). The potential performance benefits of MonetDB are impressive, particularly when considering the ultimate data volumes expected from the RSM (§2.2) and, later, from the SKA. However, its development is driven by fundamental database research and scientific user groups, and it may occasionally perform in unexpected or undesirable ways. We therefore also verify the correct operation of the TraP and, where necessary, provide "production grade" deployments using PostgreSQL, which has a long pedigree as an industry-standard database management system.

The TraP pipeline code and the Banana web interface send queries to the database using SQL. Although SQL is a standardized language[21], there is significant variation in its implementation between different database vendors: code that is written and tested against one database may unexpectedly fail when run on another system. Therefore, while the code in the TraP is designed to be standards compliant and database vendor agnostic, it is occasionally necessary to add special cases to work around different SQL dialects. To accommodate this the TraP provides a simple templating system for SQL queries. For example, we can accommodate both the PostgreSQL and MonetDB syntaxes for defining a function within the database as follows:

```
{% ifdb monetdb %}
CREATE PROCEDURE BuildFrequencyBands()
{% endifdb %}

{% ifdb postgresql %}
CREATE OR REPLACE FUNCTION BuildFrequencyBands()
RETURNS void
AS $$
{% endifdb %}

BEGIN
   -- Definition elided
END;
```

---

[16]The reference "CPython" implementation.

[17]`multiprocessing` is part of the Python standard library.

[18]http://www.celeryproject.org/

[19]http://www.monetdb.org/

[20]http://www.postgresql.org/

[21]ISO/IEC 9075-1:2011

In this way it is easy to extend the TraP's database support to encompass other systems if required.

6.4.2. Database structure

The structure of the current version of the TraP database is elaborate, consisting of many separate tables, some with tens of individual columns, complex relationships between them, and a variety of stored procedures. It is described in detail in the TraP Handbook[22]. A simplified version is shown in Fig. 5.

It is expected that, as TraP development progresses, the database will evolve to meet new requirements. For this reason, the database is versioned, and the TraP does not support mixing results across versions. The current codebase does not offer explicit support for "schema migrations" (converting a database from one version to another without losing data), although versions with this functionality have been prototyped, and off-the-shelf schema migration tools[23] may be applicable.

It is worth noting, for performance reasons, the database is not fully normalized (Kent, 1983).

6.4.3. Positional database queries

Perhaps the most common operation required of the database, both during pipeline processing (e.g. §4.4) and during later analysis is the "cone search": finding all objects of a particular type (such as source measurements, running catalogue entries) within a given search radius of a particular position. Since this operation is so common, we give it special consideration.

Given a particular target $(\alpha_\tau, \delta_\tau)$, search radius r and list of positions $(\alpha_1, \delta_1), (\alpha_2, \delta_2), ...(\alpha_n, \delta_n)$, the simplest approach to finding all the positions which fall within the radius of the target is to iterate down the list calculating for each one the great-circle distance

$$r_{\tau,n} = \arccos(\sin\delta_\tau \sin\delta_n + \cos\delta_\tau \cos\delta_n \cos|\alpha_\tau - \alpha_n|) \quad (40)$$

and selecting only those sources for which $r_{\tau,n} \leq r$. While conceptually simple, this involves multiple calculations for every source to be checked: it is prohibitively computationally expensive given a large source list.

Since this simple approach is impractical, we adopt an approach based on that described by Gray et al. (2006)[24]. This involves a hierarchical approach, filtering the list of candidate sources first on declination then on right ascension before selecting candidates based on a Cartesian dot product.

First, when any new source measurement is inserted into the database, or when the weighted mean position

---

[22]http://docs.transientskp.org

[23]For example, Alembic http://alembic.readthedocs.org/.

[24]Note that a variety of alternative approaches were considered, such as HTM (Szalay et al., 2006) and Q3C (Koposov and Bartunov, 2006); practical experience and compatibility with the database management systems informed the approach taken.

(§4.7.1) of a catalogue source is updated, we calculate a corresponding position on the unit sphere:

$$x = \cos\delta \cos\alpha \quad (41)$$
$$y = \cos\delta \sin\alpha \quad (42)$$
$$z = \sin\delta \quad (43)$$

At the same time, we define a function $\texttt{zone}(\delta)$ which maps a declination to a particular "zone", corresponding to a strip of the sky. Zones must increase monotonically with declination: $\texttt{zone}(\delta_m)$ includes all declinations falling between $\texttt{zone}(\delta_{m-1})$ and $\texttt{zone}(\delta_{m+1})$. In the current version of the TraP we use the largest integer smaller than δ as the zone, thus:

$$\texttt{zone}(\delta) = \lfloor\delta\rfloor. \quad (44)$$

However, this definition is flexible: given the constraint above, future versions could adopt a zone definition with a more fine-grained resolution or variable zone heights (e.g. chosen to provide zones of uniform area).

The Cartesian coordinates and the zone are stored in the database and are henceforth available for each running catalogue source and source measurement with no further run-time calculation.

It is next necessary to describe the 'inflation' of angular distances in right ascension with declination. For example, at a declination of $0°$, a circular region with radius θ centred on right ascension α includes RAs in the range $[\alpha-\theta, \alpha+\theta]$, whereas at a declination of $90°$ it covers the complete circle. Following Gray et al., we define the function $\texttt{alpha}(\theta, \delta)$ as

$$\texttt{alpha}(\theta, \delta) = \begin{cases} \arctan\frac{\sin\theta}{\sqrt{\cos(\delta-\theta)\cos(\delta+\theta)}} & \text{if } |\delta| + \theta < 90; \\ 180 & \text{otherwise.} \end{cases} \quad (45)$$

In general, such a circle at arbitrary α, δ can be said to cover the range $[\alpha - \texttt{alpha}(\theta, \delta), \alpha + \texttt{alpha}(\theta, \delta)]$. $\texttt{alpha}(\theta, \delta)$ is implemented as a stored procedure directly in the database so that it can be calculated for arbitrary θ and δ with minimal overhead.

These definitions made, we are now able to quickly filter the list positions to be searched. First, we calculate the maximum and minimum zones in which targets may be found, rejecting all those targets for which $\texttt{zone}(\delta_n)$ lies outside the range $[\texttt{zone}(\delta_{\tau-r}), \texttt{zone}(\delta_{\tau+r})]$. Then we reject all targets for which α_n lies outside the range $[\alpha_\tau - \texttt{alpha}(r, \delta), \alpha_\tau + \texttt{alpha}(r, \delta)]$. By ensuring that the database is appropriately indexed on $\texttt{zone}(\delta_n)$ and α this filtering can be done extremely fast.

The above filtering reduces the potentially large list of positions to match to a much more manageable size. For each position, we now check whether it lies within the required angular distance of the target. Rather than calculating the great circle distance (Eq. 40) it is more efficient to use a scalar product based on the Cartesian
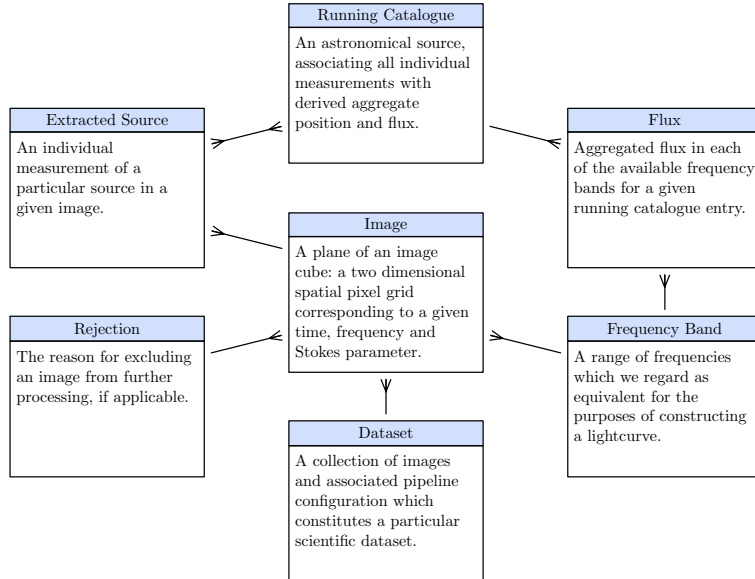
Figure 5: Simplified version of the TraP database structure. Each box represents a database table, while lines represent key-based cross-references. A single line refers to a unique key, while a split line indicates that a many-to-one relationship is possible. For example, an `Image` is a member of a single `Dataset`, but a `Dataset` may contain many `Image`s.

positions calculated according to Eqs. 41–43. Thus we check for:

$$x_\tau \cdot x_n + y_\tau \cdot y_n + z_\tau \cdot z_n \le \cos r \qquad (46)$$

Since (x_n, y_n, z_n) for each candidate is already stored in the database, the total amount of computation (and hence running time) is kept to a minimum.

The above procedure fails in the case of a discontinuity in RA: at the meridian, we jump from $359°$ to $0°$, breaking the check for α_n lying within a given range. To work around this, if a source association query crosses the meridian, we rotate the RAs of the relevant sources by $180°$ to avoid the discontinuity, perform the association as normal, and then rotate the results back to the original orientation.

6.4.4. Iteratively updating aggregate quantities

As per §4.7, we store weighted mean positions, flux densities and variability indices for all sources in the database. When a new measurement is appended to a particular running catalogue entry, it would be possible to re-calculate these quantities from scratch by averaging over all the existing information about that source in the database. This would clearly be inefficient, though. Instead, we update these quantities iteratively.

The arithmetic mean of some property x over N measurements is

$$\overline{x}_N = \frac{1}{N} \sum_{i=1}^{N} x_i \qquad (47)$$

where x_i is the ith measurement of x. When a further measurement of x is taken, updating the mean iteratively

is straightforward:

$$\overline{x}_{N+1} = \frac{N\overline{x}_N + x_{N+1}}{N+1}. \qquad (48)$$

As per §4.7.1, we also calculate the weighted mean defined as in Eq. 34. The weight of measurement x_i is w_{x_i}; the sum of all weight over N measurements is

$$W_{x_N} = \sum_{i=1}^{N} w_{x_i}. \qquad (49)$$

Given ξ_{x_N} and W_{x_N} it is then possible to express the weighted mean after $N+1$ measurements as

$$\xi_{x_{N+1}} = \frac{W_{x_N}\xi_{x_N} + w_{x_{N+1}}x_{N+1}}{W_{x_N} + w_{x_{N+1}}} \qquad (50)$$

$$= \frac{N\overline{w}_{x_N}\xi_{x_N} + w_{x_{N+1}}x_{N+1}}{N\overline{w}_{x_N} + w_{x_{N+1}}}. \qquad (51)$$

Therefore, by storing the number of measurements (N) and the average weight ($\overline{w}_{x_n}$) in addition to the weighted mean, we can iteratively update the mean and weighted mean source properties as new measurements are added to the database without revisiting all previous measurements.

As measurements are associated with catalogue sources, we keep track not only of the mean parameters but also of the evolving variability parameters, V_ν and η_ν, as described in §4.7.2.

Updating V_ν is straightforward. We store both the mean and the mean square flux density per band, $\overline{I_\nu}$ and $\overline{I_\nu^2}$ and update them using the procedure described above.

They can then be directly used to calculate V_ν based on Eq. 35.

To handle η_ν, we substitute Eq. 33 into Eq. 36 to get

$$\eta_\nu = \frac{N}{N-1} \left(\frac{1}{N} \sum_{i=1}^{N} w_{\nu,i}(I_{\nu,i} - \xi_{I_\nu})^2 \right) \tag{52}$$

$$= \frac{N}{N-1} \left(\frac{1}{N} \sum_{i=1}^{N} w_{\nu,i}(I_{\nu,i}^2 - 2I_{\nu,i}\xi_{I_\nu} + \xi_{I_\nu}^2) \right) \tag{53}$$

$$= \frac{N}{N-1} \left(\overline{w_\nu I_\nu^2} - 2\xi_{I_\nu}\overline{w_\nu I_\nu} + \xi_{I_\nu}^2 \overline{w_\nu} \right) \tag{54}$$

$$= \frac{N}{N-1} \left(\overline{w_\nu {I_\nu}^2} - \frac{\overline{w_\nu I_\nu}^2}{\overline{w_\nu}} \right) \tag{55}$$

where we use the definition of ξ_{I_ν} from Eq. 34. This quantity can be calculated directly from the aggregates stored in the database.

Every time a new association is stored in the database, the values of the variability parameters calculated at the time of association are stored together with it. In this way, it is possible to query the database for the variability parameters corresponding to any point in the history of a particular running catalogue entry.

6.5. Pixel store

Images are not created during the operation of the TraP; in general, therefore, we regard their storage as outwith the scope of TraP operations. However, it is often convenient to maintain easy access to image data which has been processed. This enables end users who are analysing the TraP results to quickly cross-check them with a visual inspection of the image data. Indeed, tools such as Banana (§5.2.2) can over-plot details of sources identified by the TraP on the image data.

In normal operation, the TraP reads images from the filesystem attached to whichever machine (or machines) upon which it is executing. Often, that filesystem is not intended as long-term image storage, but is rather a temporary resting place on whatever compute system is being used for analysis. Further, it may not always be desirable (for security or management reasons) for the ultimate scientific user of the TraP to have access to the systems upon which the pipeline runs. Finally, it is simply more convenient to aggregate images for display in one location, rather than have Banana or other tools search for them on diverse filesystems.

For these reasons, the TraP can optionally insert a copy of all pixel data it processes to a centralized store. The term "pixel data" is used deliberately: rather than storing complete image cubes, with full metadata, images are reduced to a lowest common denominator form consisting of just a pixel grid and coordinate system stored in FITS format. This enables a convenient and uniform interface by which data may be accessed for display, but does not amount to a comprehensive archive of the images.

The pixel storage used by the TraP is implemented as a MongoDB[25] database. MongoDB is a "document-oriented" database, which makes it easy to simply store and retrieve large "blobs" of binary data (such as our pixels) using a simple key-value look-up scheme.

Pixel data may be saved to the MongoDB database by the data accessor (§4.1) when it is first loaded from disk. A URL identifying the location of the corresponding pixels is then stored in the Image table of the main TraP database (Fig. 5).

6.6. Dissemination of transient notifications

After an event has been selected as scientifically noteworthy, information about it must be rapidly distributed. In general, notifications will be sent to the community at large, although it is possible that certain events may only be shared with selected partners.

Currently, the rate of transients being announced by LOFAR is low, but we anticipate it increasing in the future (Fender et al., in prep.; Stewart et al., in prep.). Looking further ahead to facilities like SKA (Dewdney et al., 2010) and LSST (Ivezić et al., 2014), it is reasonable to expect that millions of transients may be announced every day. Furthermore, rapid turn-around time for follow-up observations is often necessary. Therefore, we regard it as imperative that, as far as is possible, transient alerts can be generated, transmitted, received and acted upon without human intervention. This makes possible the development of the automatic systems that will be required to handle the upcoming transient deluge (see, for example, Staley et al., 2013).

With the above considerations in mind, we have standardized upon the VOEvent (Seaman et al., 2011) format developed by the International Virtual Observatory Alliance (IVOA) for describing transients detected by LOFAR. VOEvent provides a standardized, machine-readable way of describing a celestial event with the implication that timely follow-up is of interest. VOEvent provides mechanisms for describing:

- The facility and/or observer responsible for publishing the notification packet;

- A description of the event observed;

- Where and when the observations where made;

- Instrument specific information describing how the data was collected; and

- A scientific assessment of the event, which may be used to motivate the request for follow-up.

All of this information is presented in an XML document which can be conveniently manipulated by computer, but

---

[25]https://www.mongodb.org/

it may also be accompanied by plain text descriptions for human consumption.

The flexibility of this format is such that early LOFAR transient notifications can be simple (a position, a timestamp, a frequency and a flux density measurement, for example), and, as our understanding of both the instrumentation and the low frequency radio sky improves, the event descriptions can become increasingly elaborate and include detailed classification information and scientific assessment.

The VOEvent standard does not specify a means by which VOEvents should be transmitted from originator to recipient. However, ongoing work in the IVOA and the transient astronomy community has developed a transportation protocol (Allan and Denny, 2009) and an early version of a worldwide distribution network (Williams et al., 2012). The TKSP team has developed Comet[26] (Swinbank, 2014), an open-source implementation of this transportation system, and will use that to publish VOEvents to the distribution network. A prototype of a similar system is currently being used to notify the robotic pt5m telescope[27] of observations by AMI-LA.

7. Development methods

The TraP is a large and complex project: it consists of some tens of thousands of lines of code, written in Python and SQL, which are very different languages; it ingests image data from a variety of different sources; it interacts with two different types of database; and it is developed, tested and supported by a heterogeneous team of software developers and academic astronomers spread across multiple different institutions. Ensuring the delivery of reliable software which produces scientifically valid results under these circumstances requires a rigorous development methodology.

7.1. Planning and issue tracking

TraP releases are made at the cadence of a few per year. This provides a compromise between deploying new and upgraded features to end users as rapidly as possible, and providing a stable base which users can trust to provide consistent results from day to day while they work on a particular science project.

Releases alternate between "science" and "technical" focuses. The science-focused releases aim to deploy new and upgraded scientific analysis capabilities. Technically focused releases concentrate on consolidation of the codebase and introducing new technology, without changing the capabilities available to end users.

Goals for a release are defined through a series of "issues" targeted to a particular milestone in an issue tracker[28]. During the development cycle a daily test build is made available for commissioners. In light of development experience and results from the test build, the issues targeted for the milestone may be revised, and new issues may be added. When all the issues targeted for that milestone have been addressed, a release occurs and the cycle repeats.

7.2. Code repository and version control

The most fundamental tool in developing and maintaining a large codebase is a version control system. This is essential to maintain a list of changes to the code, including information about who changed what, when, and what the rationale was. We use the version control system to develop and test multiple variations of the TraP in parallel; to isolate and revert errors introduced to the code; and to enable the painless integration of code developed by different and geographically separate developers.

The TraP makes use of Git[29], with a central repository currently hosted on GitHub[30]. Our experience has been that software developers are quick to adapt to working with Git, but that its complexity can be off-putting to those coming from a more purely scientific background. We have organized training sessions and workshops in order to mitigate this.

7.3. Code review

In order to ensure that all code entering the codebase is of high quality, and to ensure that there is no single part of the codebase which is understood by only one developer, we require that all code contributions are reviewed by a team member other than their original author before they are added to the TraP. This process is managed using GitHub's "pull request" interface.

The overhead introduced by this review step is not negligible: the reviewer must often invest considerable time to become familiar with the code being reviewed, and sometimes a lengthy discussion between the original author and the reviewer can result. Furthermore, it can occasionally be frustrating for the author to wait for a reviewer to become available during busy times.

Despite these downsides, though, the review process has been successful: since it was instituted, the quality and reliability of the TraP codebase has increased markedly, and the entire development team has better insight into all parts of the pipeline rather than just their own particular specialization.

---

[26]http://comet.transientskp.org/
[27]https://sites.google.com/site/point5metre/

[28]For most of the lifetime of the TraP to date, this was Redmine, http:///www.redmine.org/. We have recently switched to GitHub Issues, http://www.github.com/, for better integration with our version control system.
[29]http://www.git-scm.com/
[30]http://www.github.com/

7.4. Testing and continuous integration

Testing is fundamental to the development of any software system. Mistakes are inevitable, and, in a large and complex codebase, predicting all possible effects of even simple changes becomes challenging. This is particularly the case when development takes place using a dynamic language such as Python: with no compile-time checking for type or even syntax, it is easy for errors to slip by without being noticed.

The TraP codebase is rigorously and automatically tested. At time of writing, the test suite consists of some 347 individual test cases, with three times that number of individual assertions contained within them. Test cases cover everything from 'unit' testing (checking that individual functions and procedures perform as expected when provided with both normal and extraordinary input conditions) to large scale 'integration' tests which validate the scientific results produced by large sections of the TraP on given input data. All new code must pass all of these tests (or, alternatively, explain why the test suite should be changed) before it is accepted by the code review process. Furthermore, all submissions are expected to come with their own set of tests which demonstrate their correctness.

Our testing infrastructure is based upon the `unittest` module provided as part of Python's standard library and the Jenkins[31] continuous integration system.

7.5. Documentation

Documentation is provided both for the end-user astronomer who needs to understand how to process their data and interpret the results, and for the expert user or developer who is extending the TraP to address their particular use case.

The TraP is documented using the Sphinx[32] documentation system. This can both automatically generate interface documentation from the TraP's Python code while also incorporating hand-written material giving a more complete description of the code along with tutorial-style documentation. As part of the code review process, reviewers are expected to check that code not only functions properly and is well tested, but also that, if appropriate, it is accompanied by appropriate additions or alterations to the documentation.

The documentation for all released versions of the TraP as well as the latest developmental version is available from the project website[33].

8. Integration testing

As described in §7.4, the TraP codebase is well covered by an extensive test suite which tests individual components and their interactions when provided with a variety of different inputs, based on both synthetic and archival data. Further, individual subsystems and the algorithms they implement have undergone extensive testing both in the published literature and in regular use. For example, Scheers (2011, chapter 4) describes how the source association routines were applied to cross-match the VLSS (VLA Low Frequency Sky Survey; Cohen et al., 2007), WENSS (Westerbork Northern Sky Survey; Rengelink et al., 1997) and NVSS (NRAO VLA Sky Survey; Condon et al., 1998) catalogues. This functionality forms the basis of the LOFAR Global Sky Model database (van Haarlem et al., 2013). Similarly, Spreeuw (2010, chapter 3) describes an elaborate series of statistical tests on the sourcefinder, which are expanded upon by Carbone et al. (in prep.). Results from the sourcefinder were also submitted to the ASKAP/EMU[34] Source Finding Data Challenge (Hopkins et al., in prep.); the final results of this exercise have not yet been published, but preliminary indications are that the TraP code has performed to a high standard.

Although the individual components of the TraP are well tested, it is useful to consider an integration test, which demonstrates the operation of the TraP as a coherent whole and provides an indication as to how the results may be interpreted. It is stressed that this section serves primarily as an illustration of a pipeline run under strictly controlled circumstances: we do not attempt to account for complex or unexpected behaviour of astronomical sources, as this can best be considered by comparing the source behaviour to the documented sourcefinder capabilities, database sources association behaviour, variability metrics, etc. It is worth noting that a companion paper, Rowlinson et al. (in prep.), expands upon the techniques presented here to establish strategies to determine optimal TraP configuration for a given dataset given expected source and image characteristics, while early science results derived from pre-release versions of the TraP are now becoming available (Carbone et al., submitted).

8.1. Simulation procedure

Simulated monochromatic lightcurves representing single-epoch transients observed at a frequency ν were generated. Each lightcurve consisted of 20 flux density measurements, with the flux density recorded for measurement i, $I_{\nu,i}$, given by:

$$I_{\nu,i} = \begin{cases} I_{\text{transient}} & \text{if } i = 8; \\ I_{\text{quiescent}} & \text{otherwise.} \end{cases} \tag{56}$$

The transient flux density, $I_{\text{transient}}$ was varied over the range [5, 95] Jy in steps of 5 Jy. The quiescent flux density, $I_{\text{quiescent}}$, was varied over the range $[0\,\text{Jy}, I_{\text{transient}})$ using the same step size. In this way, a total of 190 lightcurves were generated.

For each lightcurve, a set of 20 images representing LOFAR observations of the transient was simulated. In

---

order to closely mimic genuine LOFAR observations, the simulation developed was based closely on the structure of existing LOFAR visibility data. We started with visibility data obtained as part of LOFAR's Multifrequency Snapshot Sky Survey (MSSS; Heald et al., 2014). The data consisted of 20 observations of the field of 3C 295 ($14^h11^m20.6^s$, $+52°12'21''$) made between 03:00Z and 08:00Z on December 24, 2011. Each observation had an integration time of 11 minutes, and was followed by a 4 minute re-pointing time. Observation configurations were identical, covering 2 MHz of bandwidth, divided among 10 subbands and centred on 54 MHz.

We generated a model sky for the area being observed by selecting all sources from the VLSS catalogue (Cohen et al., 2007) which fall within 8° of the pointing centre and which are above a limiting flux density of 1 Jy. Spectral indices for these sources were generated by comparing the VLSS flux densities with those reported in WENSS (Rengelink et al., 1997) and NVSS (Condon et al., 1998), then used to extrapolate the source flux density to 54 MHz. Where a VLSS source had no counterpart in the other catalogues, a spectral index of -0.7 was assumed.

The simulation procedure for each image was:

1. All subbands were averaged to produce a single channel with a width of 1 MHz;
2. The stored visibilities were replaced with randomly generated Gaussian noise at a level chosen to match the System Equivalent Flux Density of the instrument (van Haarlem et al., 2013);
3. The appropriate transient flux density, based on the lightcurve being processed and the image number, was appended to the model sky at position $14^h20^m00.0^s$, $+52°00'00.0''$ (1.34° from 3C 295);
4. BBS (Loose, 2008), the standard tool use for calibrating LOFAR data, was used to simulate model visibilities and add them to the data based on a user-supplied model sky;
5. The data was calibrated and imaged as usual. The transient source was included in the model sky used for calibration. Images were generated with a radius of 6°.

The resulting images had an RMS noise level around 0.5 Jy/beam. Simulated sources with $I_{quiescent} \geq 5$ are therefore detected at around 10σ or higher in their quiescent states; sources with $I_{quiescent} = 0$ are detected when the transient turns on in image 8.

8.2. Predicted results

The flux density coefficient of variation, V_ν, and the significance of the variability, η_ν, as described in §4.7.2 were calculated independently of the pipeline machinery for each of the 190 lightcurves described in the previous section. Note that the calculation of these metrics depends not only on the raw simulated values, as described in the previous section, but also on the configuration of the pipeline run. In particular:

- When calculating η_ν (Eq. 36), we assigned an equal weight (equal to the reciprocal of the average error across all flux density measurements) to each data point.

- Only those flux density measurements recorded in or after the image of first detection are included in the variability metric calculation; as per §3, measurements from earlier images are not available during pipeline processing.

In this way, we were able to predict the variability metrics which the TraP should calculate for each source, and determine in advance which ones ought to be identified as transients for a given TraP configuration.
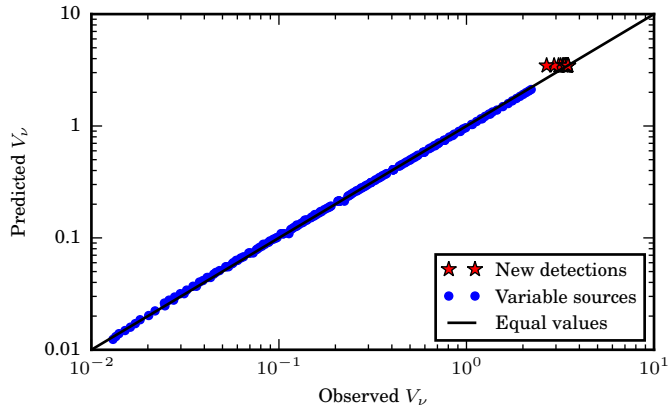
8.3. Transients pipeline results

Each dataset of snapshot images (190 datasets, 1 for each transient) was run through TraP. A near-default pipeline configuration was used: the quality control system set to not reject any images and the shape of all point sources was constrained to be equal to that of the clean beam. The variability metrics corresponding to the final snapshot for each source were extracted from the database at the end of each pipeline run. Fig. 6 shows the predicted values for each of the transient sources in comparison to the measured value by the transient pipeline. The scatter in this figure is due to three factors:

- The simulation process generates sources on a noisy background, and this noise impacts on the results produced by the sourcefinder;

- When a source is not detected by the initial sourcefinding step, the TraP's null-detection procedure (§4.5) will force a constrained fit to its position and record a (likely non-zero) flux density. The prediction procedure, by contrast, assumes a flux density of 0 Jy;

- The predicted values were calculated assuming an equal weighting for all flux density points, whereas the TraP assigns each point an independent weight.
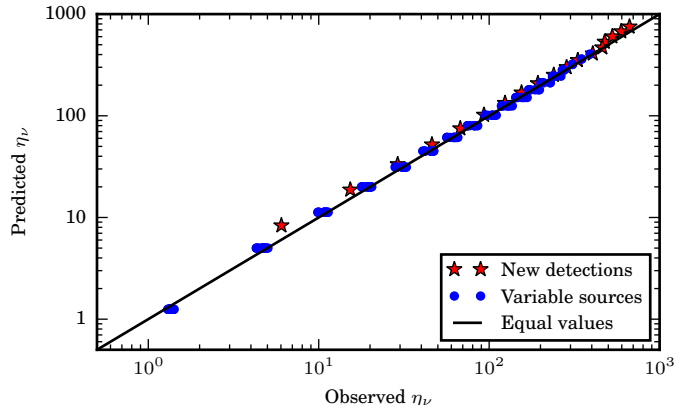
Taking these expected deviations into account, the predicted and measured values are consistent with each other. In particular, we tend to predict higher variability indices than are measured for faint sources, as our prediction procedure takes no account of image noise, assigns an equal weight to all measurements, and assigns a flux density of 0 Jy to non-detections.

As per §5.1, we distinguish between two classes of transients: *new detections* and *variable sources*. In this section we describe targeted tests which confirm that both mechanisms are performing as expected.

Throughout this section, we refer to "true positive" (TP) detections when a transient source is correctly identified as such; "false positive" (FP) detections when a non-transient

(a) Flux density coefficient of variation (V_ν).

(b) Significance of the flux density variability (η_ν).

Figure 6: Comparison of predicted and measured variability parameters for simulated transients.

source is incorrectly labelled as transient, and "false negative" (FN) detections when a transient source is incorrectly labelled as non-transient. We then define

$$\text{Precision} = \frac{\text{TP}}{\text{TP} + \text{FP}} \quad \text{and} \quad (57)$$

$$\text{Recall} = \frac{\text{TP}}{\text{TP} + \text{FN}}. \quad (58)$$

Following these definitions, the *precision* of the result is the fraction of the total number of detections which are correct and the *recall* is the fraction of the total number of transients which were correctly identified. The best possible TraP performance is obtained by maximizing both the precision and the recall.

8.3.1. New detections

We selected all sources from the database that were initially detected in any image except the first. Following the procedure described in §5.1.1, and using a margin of 3σ, we classified them as either not transient (i.e. below previous detection threshold), marginally transient (above previous detection threshold in the lowest-noise portion of at least one previous image) or likely transient (above previous detection threshold in the highest-noise portion of at least one previous image). We find that:

- Likely transients are recovered with a precision of 1.0 and recall of 0.94;

- Marginal transients are recovered with a precision of 0.02 and recall of 1.0.

Based on the simplified test described here, we conclude that the algorithm used to detect likely transients provides a robust way of identifying many transients with a high resistance to false positives. Further, since all lightcurve data is retained in the database, the list of marginal transients provides a key starting point for future manual checking and data mining.

An important limiting factor in this test is the limited resolution at which the noise maps are stored (i.e. just a "best" and "worst" value for each image). Recording noise at a more fine-grained level would enable us to significantly increase the precision with which possible transients are identified. This is a possible area of future TraP development (§10).
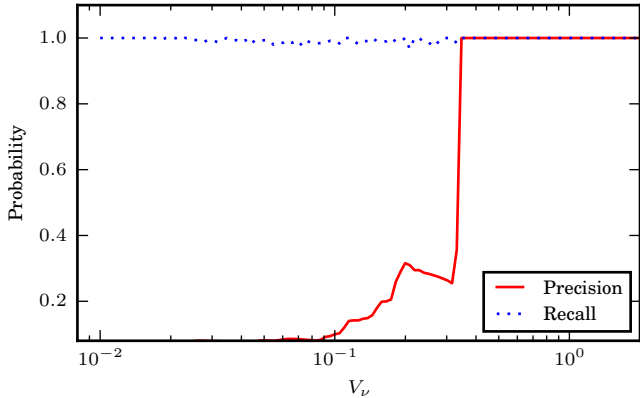
8.3.2. Variable sources

We selected all sources which were initially observed in the first image (i.e. they were not candidates for being marked as new detections) and which had values of η_ν and V_ν greater than 0.1 and 0.01 respectively. We constructed an equivalent list based on the simulation inputs and known image noise level; note that this list excludes some transient sources which fall below the detection threshold. By combining these lists, we can calculate the precision and recall (Eqs. 57 & 58) as a function of the variability parameters. These are plotted in Fig. 7. Above some limiting value of each threshold, there are no positive detections (either true or false) so the values of Eqs. 57 and 58 are undefined; the plots are truncated at this point. Note that for values of $\eta_\nu \geq 1$ and $V_\nu \geq 0.3$ the precision is 1.0: no false positives are recorded. Below these values, precision drops rapidly due to noise-based variation of stable sources.
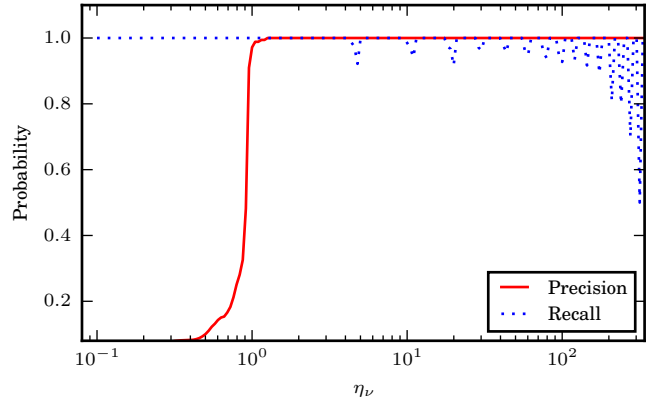
For all values of η_ν and V_ν the recall is similarly close to 1.0. Variations are due to uncertainties introduced by the simulation and measurement process, which occasionally cause the measured value of the transient parameters to drop below their predicted values.

9. Run-time performance

As described in sections 2.2 and 3, the TraP is ultimately intended to perform near real-time analysis of streaming image data. Although the required rapid imaging capability is not yet available from LOFAR, we anticipate that other projects—most notably AARTFAAC (Prasad and Wijnholds, 2012)—will provide streaming image data in

(a) Probabilities as a function of the threshold applied to the flux density coefficient of variation (V_ν).

(b) Probabilities as a function of the threshold applied to the significance of the flux density variability (η_ν).

Figure 7: The precision and recall probabilities as functions of the triggering thresholds for the variability metrics V_ν and η_ν.

the relatively near future. It is therefore instructive to consider to what extent the run-time performance of the TraP is adequate to address such a data stream.

It is worth emphasizing that TraP development to date has focused on correctness rather than performance. Our aim has been to produce a robust and well-tested codebase that can then be optimized to address real-time data processing. We strive to adopt fundamental algorithms which show benign scaling characteristics to large numbers of images and sources, but emphasize that the codebase still provides ample opportunity for optimization.

Broadly, we split our consideration of performance characteristics into two parts, corresponding to the two most computational expensive parts of the TraP. In §9.1 we focus on the performance of the Python code, and particularly that of the computationally intensive source finding algorithms. In §9.2 we turn to the matter of inserting and associating measurements in the database and the calculation of per-source aggregates.

Throughout, we emphasize that there are a large number of tunable parameters in this analysis, both in terms of the pipeline configuration and the characteristics of the test data; here, we only give an overview of likely scaling considerations. For a detailed review of the sourcefinder performance refer to Carbone et al. (in prep.), and for an in-depth discussion of database characteristics see Scheers et al. (in prep.).

Throughout this section, the times reported correspond to Python code running on an Intel Xeon E5-2660v2 CPU with a maximum clock speed of 2.2 GHz and, where applicable, interoperating with PostgreSQL 9.3.5 running on an AMD Opteron 2384 with a maximum clock speed of 2.7 GHz. We configured PostgreSQL to make better use of the available system resources by increasing its working memory (to 100 MB), its shared buffer (to 2048 MB) and its checkpoint interval to 32 segments.
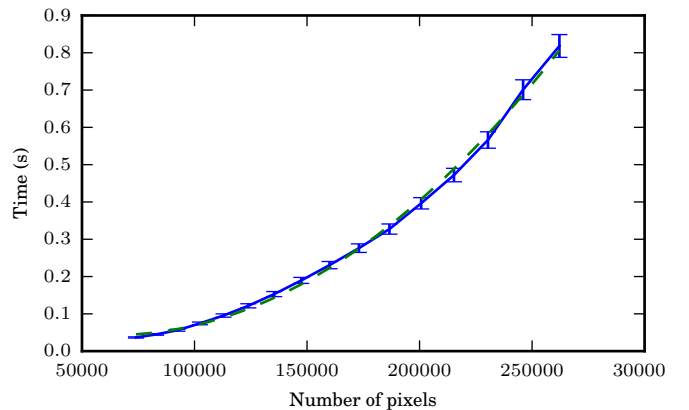

Figure 8: Time taken to calculate the background and RMS maps as a function of the number of pixels in the image. The solid line shows the mean measured time over 3800 test images; the dashed line, a quadratic fit to the data.

9.1. Sourcefinder performance

Based on the discussion in §4.3, we divide the operation of the sourcefinder into two major components: the calculation of per-image background and RMS maps, then the identification and measurement of sources within the image. The former depends on the size of the image, but is independent of the number of sources within it; the latter increases with source count.

For each of the 3800 images simulated as described in §8.1 the time taken to generate background and RMS maps covering the whole image was measured. The edges of the images were then masked, and timing repeated for maps covering only the unmasked portion. This process was repeated until only a small fraction of the image was left unmasked. The times recorded are shown in Fig. 8. For comparison, we also plot the results of a least squares
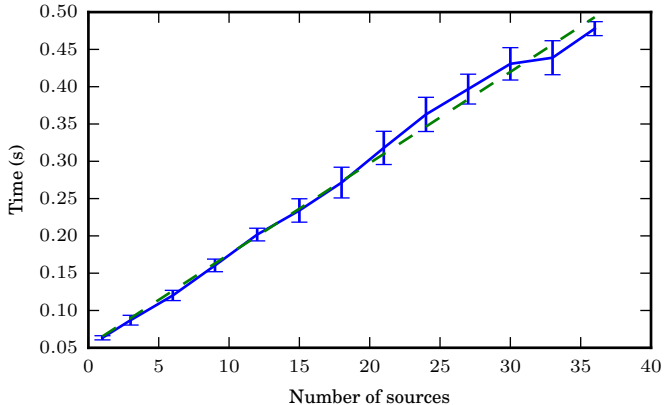
24

Figure 9: Time taken to find and measure the sources in an image as a function of the number of sources found. The solid line shows the mean time measured over 3800 test images; the dashed line a linear fit to the data.

quadratic fit to the data:

$$t_{\mathrm{map}} = 1.9 \times 10^{-11} p^2 - 2.5 \times 10^{-6} p + 0.1 \, \mathrm{s}, \qquad (59)$$

where t_{map} is the time taken to process p pixels. While the detailed values are system dependent, it is important to note that the algorithm scales as $\mathcal{O}(N^2)$ in number of pixels.

As the unmasked area of each image is decreased, the number of sources which can be detected and measured within the image also decreases. For each portion of each image we performed a source finding and measurement step with a detection threshold of 10σ. The sourcefinder was configured not to deblend sources (§4.3.3), and to constrain the shape of the resulting measurements to be equal to the restoring beam (§4.3.5).

Fig. 9 records the total time taken to identify and fit all the sources in an image as a function of the source number. A linear least squares fit to the data provides the expression

$$t_{\mathrm{fit}} = 0.012n + 0.053 \, \mathrm{s} \qquad (60)$$

for the t_{fit} taken to identify and measure n sources. While again the detailed timings are system-dependent, the key point is the scaling as $\mathcal{O}(N)$ with number of sources.

9.2. Database performance

There are two important axes along which database performance could vary. The first is with number of images processed: as more data is stored, the number of source measurements which must be associated and the number of data points of which aggregates must be calculated increases. For use in a long term monitoring programme, we require that this accumulation of data does not cause the database to become slower with time. Secondly, we consider performance as a function of the number of sources per image: more measurements increase not only the number of
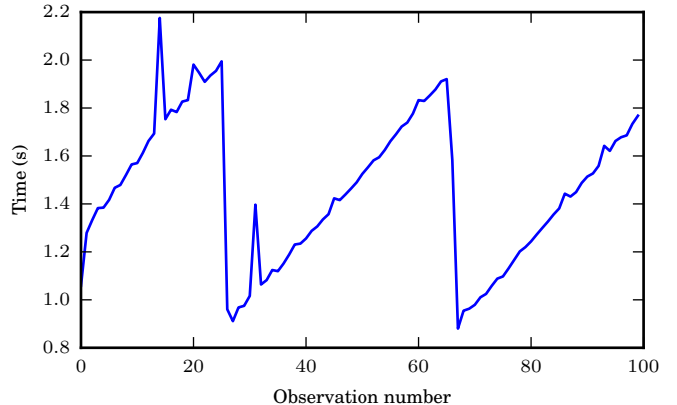

Figure 10: Time taken to process each simulated observation with a population of 1100 sources in the database.

aggregates to be calculated but also the number of potential source associations.

Artificial source lists representing an artificial sky at arbitrary frequency and pointing and covering a circular region of radius 20° were constructed. Sources were placed on a regular grid within the region. Each source was assumed to be a point source, and assigned a random flux density in the range 1–10 Jy from a uniform distribution. Sixteen such source lists were created, containing between 50 and 1200 sources in increments of 50.

For each source population, a set of 100 source measurements was constructed by perturbing the source position with a Fisher distribution (Fisher, 1953) with concentration parameter $\kappa = 2 \times 10^9$, chosen to approximate the systematic position uncertainty of around 5" which we have observed to be typical in LOFAR images (Carbone et al., in prep.). This simulates an observation of the source population.

For each source population, each simulated observation in turn was inserted and processed (including source association and calculation of aggregate parameters by the database). The time taken to perform all database operations was recorded.

In Fig. 10 we show the time taken to perform all the processing of each simulated observation of 1100 sources as a function of image number; a similar pattern is observed for all other source counts. The characteristic "saw tooth" pattern in the figure is due to PostgreSQL periodically checkpointing its write ahead log; other minor variations are explained by internal housekeeping tasks running within the database and by varying system and network load over the course of the test. The key result, though, is that there is no evidence of a systematic increase in processing time with observation number.

In Fig. 11 we show the mean time taken to perform all the processing of each simulated observation as a function of source count. For comparison, we also plot the expression

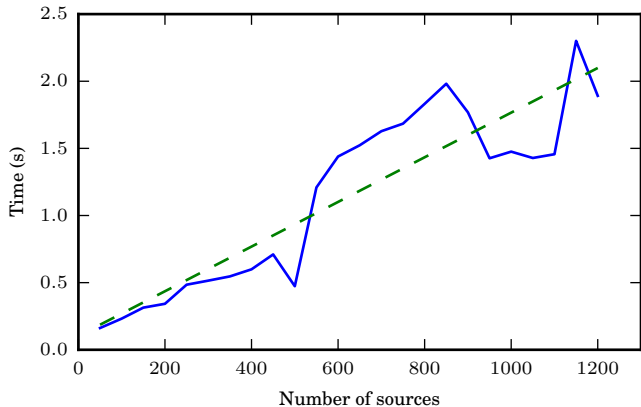$$t_{\mathrm{db}} = 0.0017n + 0.10 \, \mathrm{s} \qquad (61)$$

Figure 11: Time taken by the database to process a simulated observation as a function of number of sources in the observation. The solid line shows the mean value over 100 test observations; the dashed line, a linear function for comparison.

where t_{db} is the time taken to process a simulated observation of n sources. The detailed timings are, again, system dependent, but it is important to note the scaling as $\mathcal{O}(N)$ with number of sources per observation.

9.3. Practical performance considerations

We conclude this discussion of pipeline runtime performance by comparing the measured TraP performance to potential LOFAR transient monitoring strategies.

The initial Radio Sky Monitor strategy (Fender et al., in prep.) is to use six beams from LOFAR to tile out a wide area on the sky. Each beam consists of four frequency bands, which are imaged separately. Assuming LOFAR is operating in 8 bit mode (§2.1), each band contains 20 subbands and provides a bandwidth of 3.6 MHz.

In Tab. 2 we list the parameters of each of six major LOFAR observing modes and provide the full width at half maximum and the angular resolution of a single image constructed using the survey strategy described. The observing modes include using only the core LOFAR stations, using the full Dutch LOFAR array, and using only that subset of the full array which contains baselines no more than 6 km in length. This latter configuration has been shown to provide a good compromise between image fidelity and processing time in early LOFAR observations and has been used for initial RSM observations.

In Tab. 3 we provide estimates of the 5σ detection limit and corresponding source count for each of the configurations at a range of integration times. Sensitivity and confusion limits were estimated using the online LOFAR Image Noise Calculator[35]. Following current standard LOFAR observing practice, when using the high band remote stations were "tapered", reducing sensitivity while increasing field of view to match that of the stations in the core.

---

[35]Version 0.31; `http://www.astron.nl/~heald/test/sens2.php`

Where possible, source counts were taken from preliminary analysis of LOFAR RSM data (Fender et al., in prep.); otherwise, they were estimated by extrapolating from other surveys assuming a spectral index of -0.7: for each configuration, the survey best approximating the spatial resolution was selected from FIRST (Faint Images of the Radio Sky at Twenty-cm; Becker et al., 1994), NVSS (Condon et al., 1998), VLSS (Cohen et al., 2007) and WENSS (Rengelink et al., 1997).

Also in Tab. 3 we estimate the processing time for each image through both the sourcefinder ($t_{\mathrm{map}} + t_{\mathrm{fit}}$) and the database ($t_{\mathrm{db}}$). Note that these equations reflect the particular characteristics of the systems used for benchmarking and can provide only guideline performance estimates. Further note that this estimate includes only the major pipeline components identified above; it is reasonable to expect modest overheads from other parts of the pipeline.

Note that for most image types excluding the full array the processing time per image is considerably less than the integration time for that image. This indicates that processing a real-time stream of images of this type is tractable on the systems used for benchmarking.

As described above, the likely operation configuration consists not of a single image stream but of four bands in each of six beams: a factor of 24 greater than the figures quoted. For all 1 s, and some longer, integrations, this increases the total processing time to greater than the integration time. However, three factors mitigate this:

- As described in §6.3, we support parallel (and, optionally, distributed) sourcefinder operation: by distributing the processing time required over multiple CPUs, we achieve a near-linear reduction in wall-clock time.

- By starting to search for sources in timestep t_{n+1} before timestep t_n has finished processing, we can ensure that both sourcefinding and database systems are efficiently occupied, rather than synchronously waiting for each other.

- The hardware platform used for benchmarking the database is several years old; more powerful systems are now available which will provide a significant constant factor improvement in database throughput.

We also emphasize that the real-time LOFAR imaging mode is still under development (§2.2): all current processing is carried out off-line. The run-time performance of the TraP is significantly better than that of the imaging tools used to provide it with input in this mode.

Finally, we reiterate that TraP development to date has focused on correctness over performance. There is much still to be gained in terms of optimization of individual algorithms, efficiency of implementation (e.g. replacing core Python loops with Cython equivalents) and best exploiting the performance of high level tools (e.g. the potential gains of the MonetDB system over PostgreSQL as described in §6.4.1).

Configuration name	Freq. (MHz)	BW (MHz)	Num. stations Core	Remote	Max. baseline (km)	FWHM (deg.)	Ang. res. (asec.)	Pixels per image
LBA core only	60	3.6	24	0	3.5	9.8	294.7	1.0×10^5
LBA 6 km baselines	60	3.6	24	4	6.0	9.8	171.9	3.0×10^5
LBA NL array	60	3.6	24	16	121.0	9.8	8.5	1.2×10^8
HBA core only	150	3.6	24	0	3.5	3.8	117.9	9.5×10^4
HBA 6 km baselines	150	3.6	24	4	6.0	3.8	68.8	2.8×10^5
HBA NL array	150	3.6	24	16	121.0	3.8	3.4	1.1×10^8

Table 2: Parameters of LOFAR observing modes. For each mode, we quote the angular resolution and full width at half maximum of a single beam and a bandwidth of 3.6 MHz, equivalent to 20 subbands.

Configuration name	Integration time (s)	5σ detection limit (mJy/beam)	Source count Origin	Number	Processing time (s) Sourcefinder	Database
LBA core only	1	2346.5	VLSS	27.6	0.46	0.15
	10	$\mathcal{C}$ 1066.3	VLSS	90.0	1.22	0.25
LBA 6 km baselines	1	2005.1	VLSS	34.9	1.58	0.16
	10	634.1	VLSS	196.3	3.55	0.42
	100	$\mathcal{C}$ 465.0	VLSS	312.6	4.98	0.62
LBA NL array	1	1395.8	VLSS	60.1	2.86×10^5	0.20
	10	441.4	VLSS	337.9	2.86×10^5	0.67
	100	139.6	RSM	761.3	2.86×10^5	1.37
	1000	44.2	WENSS	2043.6	2.86×10^5	3.50
	10000	14.0	FIRST	3537.0	2.86×10^5	5.99
HBA core only	1	$\mathcal{C}$ 137.0	LOFAR	45.3	0.67	0.18
HBA 6 km baselines	1	102.0	LOFAR	70.5	1.86	0.22
	10	$\mathcal{C}$ 59.7	LOFAR	157.4	2.92	0.37
HBA NL array	1	82.8	LOFAR	96.4	2.53×10^5	0.26
	10	26.2	WENSS	323.0	2.53×10^5	0.64
	100	8.3	FIRST	449.5	2.53×10^5	0.85
	1000	2.6	FIRST	2516.8	2.53×10^5	4.29
	10000	0.8	FIRST	14153.5	2.53×10^5	23.64

Table 3: Source counts and processing times predicted for a single image using each of the LOFAR configurations described in Tab. 2 at a range of integration times. The symbol $\mathcal{C}$ indicates that the detection limit was set by confusion noise rather than image sensitivity.

10. Releases and future development

This manuscript describes release 2.0 of the TraP, dating from December 2014. With this release, the TraP became an open source project, and therefore freely available to download from our GitHub repository[36] under a two-clause BSD-style[37] license. If you use the TraP, or code derived from it, in a paper or other publication, we request that you cite this work.

After this release, development will continue. Future releases of the TraP are expected to expand upon the current functionality to offer features such as:

- Performance optimization in support of real-time streaming transient monitoring;

- Automatic preliminary classification of detected transients;

- Support for multi-terabyte lightcurve archives and enhanced archive data-mining and visualization;

- Automatic cross-correlation of TraP detected sources with known catalogue sources across a range of wavelengths;

- Improved methods for apportioning flux density from a single measurement among multiple sources on association;

- Full Stokes support, for both identifying and classifying sources;

- Higher resolution and more flexible noise maps;

- Construction and usage of a deep average image of the surveyed area.

11. Conclusions

The current and next generation of astronomical survey facilities, across a wide range of wavelengths but particularly in the radio, provide an opportunity to explore the transient and variable sky in powerful and unprecedented ways. This is especially true of LOFAR, which combines a remarkably wide field of view with unique sensitivity to low radio frequencies and a flexible, software-driven architecture. However, identifying transients in the massive data volumes produced by these instruments is challenging.

This manuscript has described our attempt to rise to this challenge in the form of the LOFAR Transients Pipeline. It combines a flexible, high-performance architecture with robust analysis tools in a well tested and documented package. We have shown how it can both be used to generate alert messages as new transients are discovered and to populate a database of lightcurves of potential transients for offline analysis. We have demonstrated that it is capable of accurately recovering a known population of transients from simulated LOFAR observations.

The TraP is now being used in support of ongoing LOFAR observing campaigns. However, development continues, and we are actively expanding its capabilities, both to better address ongoing LOFAR operations and to increase its applicability to other instruments and wavelength regimes. The codebase is open source and freely available; we actively invite you to join us in improving it.

12. Acknowledgements

References

Alard, C., Lupton, R. H., Aug. 1998. A Method for Optimal Image Subtraction. Astrophys. J. 503, 325–331.

Allan, A., Denny, R. B., Aug. 2009. VOEvent Transport Protocol, Version 1.1. Note, International Virtual Observatory Alliance.

Amdahl, G. M., 1967. Validity of the single processor approach to achieving large scale computing capabilities. In: Proceedings of the April 18-20, 1967, Spring Joint Computer Conference. AFIPS '67 (Spring). ACM, New York, NY, USA, pp. 483–485.

Anderson, G. E., et al., 2014. Probing the bright radio flare and afterglow of GRB 130427A with the Arcminute Microkelvin Imager. Mon. Not. R. Astron. Soc. 440, 2059–2065.

Astropy Collaboration, et al., Oct. 2013. Astropy: A community Python package for astronomy. Astron. Astrophys. 558, A33.

Atwood, W. B., et al., Jun. 2009. The Large Area Telescope on the Fermi Gamma-Ray Space Telescope Mission. Astrophys. J. 697, 1071–01102.

Bannister, K. W., et al., Mar. 2011. A 22-yr southern sky survey for transient and variable radio sources using the Molonglo Observatory Synthesis Telescope. Mon. Not. R. Astron. Soc. 412, 634–664.

Banyer, J., Murphy, T., the VAST Collaboration, 2012. VAST – a real-time pipeline for detecting radio transients and variables on the Australian SKA Pathfinder (ASKAP) telescope. In: Ballester, P. (Ed.), Astronomical Data Analysis Software and Systems XXI. Vol. 461 of Astronomical Society of the Pacific Conference Series. p. 725.

Becker, R. H., White, R. L., Helfand, D. J., 1994. The VLA's FIRST Survey. In: Crabtree, D. R., Hanisch, R. J., Barnes, J. (Eds.), Astronomical Data Analysis Software and Systems III. Vol. 61 of Astronomical Society of the Pacific Conference Series. p. 165.

Bell, M. E., et al., 2011. An automated archival Very Large Array transients survey. Mon. Not. R. Astron. Soc. 415, 2–10.

Bell, M. E., et al., Feb. 2014. A survey for transients and variables with the Murchison Widefield Array 32-tile prototype at 154 MHz. Mon. Not. R. Astron. Soc. 438, 352–367.

---

[36] https://github.com/transientskp/tkp/
[37] http://opensource.org/licenses/BSD-2-Clause

[38] http://www.nlesc.nl/

Benjamini, Y., Hochberg, Y., 1995. Controlling the false discovery rate: a practical and powerful approach to multiple testing. J. Roy. Statist. Soc. Ser. B 57, 289–300.

Bertin, E., Arnouts, S., Jun. 1996. SExtractor: Software for source extraction. Astron. Astrophys. Suppl. Ser. 117, 393–404.

Bolch, B. W., 1968. More on unbiased estimation of the standard deviation. The American Statistician 22, 27.

Booth, R. S., Jonas, J. L., Mar. 2012. An Overview of the MeerKAT Project. African Skies 16, 101.

Bower, G. C., et al., Oct. 2011. The Allen Telescope Array Pi GHz Sky Survey II. Daily and Monthly Monitoring for Transients and Variability in the Boötes Field. Astrophys. J. 739, 76.

Broderick, J., et al., in prep.

Brown, T. M., et al., Sep. 2013. Las Cumbres Observatory Global Telescope Network. Publ. Astron. Soc. Pac. 125, 1031–1055.

Carbone, D., et al., in prep. PySE: Software for Extracting Sources from LOFAR Radio Telescope Images.

Carbone, D., et al., submitted. New methods to constrain the radio transient rate: results from a survey of four fields with LOFAR.

Codd, E. F., Jun. 1970. A relational model of data for large shared data banks. Commun. ACM 13, 377–387.

Coenen, T., et al., Oct. 2014. The LOFAR pilot surveys for pulsars and fast radio transients. Astron. Astrophys. 570, A60.

Cohen, A. S., et al., Sep. 2007. The VLA Low-Frequency Sky Survey. Astron. J. 134, 1245–1262.

Condon, J. J., 1997. Errors in elliptical Gaussian fits. Publ. Astron. Soc. Pac. 109, 166–172.

Condon, J. J., et al., May 1998. The NRAO VLA Sky Survey. Astron. J. 115, 1693–1716.

Croft, S., et al., Apr. 2011. The Allen Telescope Array Twenty-centimeter Survey—A 700-square-degree, Multi-epoch Radio Data Set. II. Individual Epoch Transient Statistics. Astrophys. J. 731, 34.

de Bruyn, A. G., Bernardi, G., Lofar Eor-Team, Sep. 2009. The First Deep WSRT 150 MHz Full Polarization Observations. In: Saikia, D. J., Green, D. A., Gupta, Y., Venturi, T. (Eds.), The Low-Frequency Radio Universe. Vol. 407 of Astron. Soc. Pac. Conf. Ser. p. 3.

de Ruiter, H. R., Willis, A. G., Arp, H. C., May 1977. A Westerbork 1415 MHz survey of background radio sources. II - Optical identifications with deep IIIA-J plates. Astron. Astrophys. Suppl. Ser. 28, 211–293.

Denneau, L., et al., Apr. 2013. The Pan-STARRS Moving Object Processing System. Publ. Astron. Soc. Pac. 125, 357–395.

Dent, W. A., Jun. 1965. Quasi-Stellar Sources: Variation in the Radio Emission of 3C 273. Science 148, 1458–1460.

Dewdney, P., et al., 2010. SKA Memo 130: SKA Phase 1: Preliminary System Description.

Drake, A. J., et al., May 2009. First Results from the Catalina Real-Time Transient Survey. Astrophys. J. 696, 870–884.

Fender, R., et al., 2006. The LOFAR Transients Key Project. In: Proceedings of the VI Microquasar Workshop: Microquasars and Beyond. PoS(MQW6)014.

Fender, R., et al., in prep. The LOFAR Radio Sky Monitor.

Fender, R. P., Bell, M. E., Sep. 2011. Radio transients: an antediluvian review. Bulletin of the Astronomical Society of India 39, 315–332.

Fisher, R., 1953. Dispersion on a sphere. Proc. Roy. Soc. London Ser. A. 219, 295–305.

Fishman, G. J., 1992. BATSE – The burst and transient source experiment on the Gamma Ray Observatory. pp. 265–272.

Frail, D. A., Kulkarni, S. R., Bloom, J. S., Mar. 1999. An outburst of relativistic particles from the soft γ-ray repeater SGR1900+14. Nature 398, 127–129.

Frail, D. A., et al., Sep. 1997. The radio afterglow from the γ-ray burst of 8 May 1997. Nature 389, 261–263.

Frail, D. A., et al., Mar. 2012. A revised view of the transient radio sky. Astrophys. J. 747, 70.

Freund, J. E., Williams, F. J., 2010. Outline of Basic Statistics: Dictionary and Formulas. Courier Corporation.

Gaensler, B. M., Hunstead, R. W., Apr. 2000. Long-term Monitoring of Molonglo Calibrators. Publ. Astron. Soc. Aus. 17, 72–82.

Gautschi, W., 1972. Error function and Fresnel integrals. Dover.

Gehrels, N., et al., Aug. 2004. The Swift Gamma-Ray Burst Mission. Astrophys. J. 611, 1005–1020.

Graham, M., et al., May 2014. Employing SimpleTimeSeries for representing time series, version 1.0. Note, International Virtual Observatory Alliance.

Gray, J., Nieto-Santisteban, M. A., Szalay, A. S., 2006. The Zones Algorithm for Finding Points-Near-a-Point or Cross-Matching Spatial Datasets. MSR TR 2006 52, Microsoft and The Johns Hopkins University.

Gregory, P. C., et al., Oct. 1972. The nature of the first Cygnus X-3 radio outburst. Nature Physical Science 239, 114–117.

Greisen, E. W., Mar. 2003. AIPS, the VLA, and the VLBA. Information Handling in Astronomy - Historical Vistas 285, 109.

Hancock, P. J., et al., May 2012. Compact continuum source finding for next generation radio surveys. Mon. Not. R. Astron. Soc. 422, 1812–1824.

Harmon, B. A., et al., Jan. 2002. The Burst and Transient Source Experiment Earth Occultation Technique. Astrophys. J., Suppl. Ser. 138, 149–183.

Heald, G., et al., Aug. 2010. Progress with the LOFAR Imaging Pipeline. In: Proceedings of the ISKAF2010 Science Meeting. PoS(ISKAF2010)057.

Heald, G., et al., Dec. 2011. LOFAR: Recent Imaging Results and Future Prospects. Journal of Astrophysics and Astronomy 32, 589–598.

Heald, G., et al., 2014. The LOFAR Multifrequency Snapshot Sky Survey (MSSS): 1. Survey description and first results. Astron. Astrophys.Submitted.

Hendricks, W. A., Robey, K. W., 1936. The sampling distribution of the coefficient of variation. The Annals of Mathematical Statistics 7 (3), 129–132.

Högbom, J. A., 1974. Aperture Synthesis with a non-regular distribution of interferometer baselines. Astron. Astrophys. Suppl. Ser. 15, 417–426.

Hopkins, A. M., et al., Feb. 2002. A New Source Detection Algorithm Using the False-Discovery Rate. Astron. J. 123, 1086–1094.

Hopkins, A. M., et al., Feb. 2003. The Phoenix Deep Survey: The 1.4 GHz Microjansky Catalog. Astron. J. 125, 465–477.

Hopkins, A. M., et al., in prep. The ASKAP/EMU Source Finding Data Challenge.

Hunter, J. D., 2007. Matplotlib: A 2d graphics environment. Computing In Science & Engineering 9 (3), 90–95.

Idreos, S., et al., Mar. 2012. MonetDB: Two Decades Of Research In Column-Oriented Database Architectures. IEEE Data Engineering Bulletin 35 (1), 40–45.

Ivezić, Ž., et al., 2014. LSST: From science drivers to reference design and anticipated data products, version 3.1. arXiv:0805.2366.

Jenet, F. A., Gil, J., 2003. Using the intensity modulation index to test pulsar radio emission models. The Astrophysical Journal Letters 596 (2), L215.

Kent, W., Feb. 1983. A simple guide to five normal forms in relational database theory. Commun. ACM 26 (2), 120–125.

Kesteven, M. J. L., Bridle, A. H., Brandie, G. W., Aug. 1977. Variability of extragalactic sources at 2.7 GHz. III - The nature of the variations in different source classes. Astron. J. 82, 541–556.

Koposov, S., Bartunov, O., Jul. 2006. Q3C, Quad Tree Cube – The new sky-indexing concept for huge astronomical catalogues and its realization for main astronomical queries (cone search and xmatch) in Open Source Database PostgreSQL. In: Gabriel, C., Arviset, C., Ponz, D., Enrique, S. (Eds.), Astronomical Data Analysis Software and Systems XV. Vol. 351 of Astronomical Society of the Pacific Conference Series. p. 735.

Lande, R., 1977. On comparing coefficients of variation. Systematic Biology 26 (2), 214–217.

Law, C. J., et al., Nov. 2011. Millisecond Imaging of Radio Transients with the Pocket Correlator. Astrophys. J. 742, 12.

Law, N. M., et al., Dec. 2009. The Palomar Transient Factory: System Overview, Performance, and First Results. Publ. Astron. Soc. Pac. 121, 1395–1408.

Levan, A. J., et al., Jul. 2011. An extremely luminous panchromatic

outburst from the nucleus of a distant galaxy. Science 333, 199–202.

Levine, A. M., et al., Sep. 1996. First Results from the All-Sky Monitor on the Rossi X-Ray Timing Explorer. Astrophys. J. 469, L33.

Loose, G. M., Aug. 2008. LOFAR Self-Calibration Using a Blackboard Software Architecture. In: Argyle, R. W., Bunclark, P. S., Lewis, J. R. (Eds.), Astronomical Data Analysis Software and Systems XVII. Vol. 394 of Astronomical Society of the Pacific Conference Series. p. 91.

Lyubarsky, Y., Jul. 2014. A model for fast extragalactic radio bursts. Mon. Not. R. Astron. Soc. 442, L9–L13.

McDowell, J., et al., Feb. 2015. IVOA Spectral Data Model, Version 2.0. Proposed Recommendation, International Virtual Observatory Alliance.

McKay, A. T., 1932. Distribution of the coefficient of variation and the extended "t" distribution. Journal of the Royal Statistical Society 95 (4), 695–698.

Meegan, C., et al., Sep. 2009. The Fermi Gamma-ray Burst Monitor. Astrophys. J. 702, 791–804.

Mooley, K. P., et al., May 2013. Sensitive Search for Radio Variables and Transients in the Extended Chandra Deep Field South. Astrophys. J. 768, 165.

Moré, J. J., 1977. The Levenberg-Marquardt algorithm: Implementation and theory. In: Watson, G. A. (Ed.), Numerical Analysis. Vol. 630 of Lecture Notes in Mathematics. pp. 105–116.

Murphy, T., et al., Feb. 2013. VAST: An ASKAP Survey for Variables and Slow Transients. Publ. Astron. Soc. Aus. 30, 6.

Narayan, R., Oct. 1992. The Physics of Pulsar Scintillation. Royal Society of London Philosophical Transactions Series A 341, 151–165.

Nijboer, R. J., Pandey-Pommier, M., de Bruyn, A. G., 2009. LOFAR imaging capabilities and system sensitivity. Memo 113, Square Kilometre Array Project.

O'Mullane, W., et al., Feb. 2005. Batch is back: CasJobs, serving multi-TB data on the Web. eprint arXiv:cs/0502072.

Pérez, F., Granger, B. E., May 2007. IPython: a system for interactive scientific computing. Computing in Science and Engineering 9 (3), 21–29.

Prasad, P., Wijnholds, S. J., May 2012. AARTFAAC: Towards a 24x7, All-sky Monitor for LOFAR. In: Proceedings of 'New Windows on Transients across the Universe': A discussion meeting of the Royal Society, London.

Rau, A., et al., Dec. 2009. Exploring the Optical Transient Sky with the Palomar Transient Factory. Publ. Astron. Soc. Pac. 121, 1334–1351.

Rengelink, R. B., et al., Aug. 1997. The Westerbork Northern Sky Survey (WENSS). I. A 570 square degree Mini-Survey around the North Ecliptic Pole. Astron. Astrophys. Suppl. Ser. 124, 259–280.

Rickett, B. J., 1990. Radio propagation through the turbulent interstellar plasma. Ann. Rev. Astron. Astrophys. 28, 561–605.

Rowlinson, A. R., et al., in prep. Methodology for optimising the LOFAR Transients Pipeline. Astron. Comp.

Rutledge, R. E., Brunner, R. J., Prince, T. A., Lonsdale, C., Nov. 2000. XID: Cross-Association of ROSAT/Bright Source Catalog X-Ray Sources with USNO A-2 Optical Point Sources. Astrophys. J., Suppl. Ser. 131, 335–353.

Sagiv, A., Waxman, E., Aug. 2002. Collective Processes in Relativistic Plasma and Their Implications for Gamma-Ray Burst Afterglows. Astrophys. J. 574, 861–872.

Scheers, L. H. A., 2011. Transient and Variable Radio Sources in the LOFAR Sky. Ph.D. thesis, University of Amsterdam.
URL http://hdl.handle.net/11245/1.328956

Scheers, L. H. A., et al., in prep. LOFAR Transients Key Project Archival Database.

Seaman, R., et al., Jul. 2011. Sky event reporting metadata, version 2.0. Recommendation, International Virtual Observatory Alliance.

Spreeuw, J. N., 2010. Search and detection of low frequency radio transients. Ph.D. thesis, University of Amsterdam.
URL http://hdl.handle.net/11245/1.324881

Staley, T. D., et al., 2013. Automated rapid follow-up of Swift gamma-ray burst alerts at 15 GHz with the AMI Large Array. Mon. Not.

R. Astron. Soc. 428, 3114–3120.

Stappers, B. W., et al., Jun. 2011. Observing pulsars and fast transients with LOFAR. Astron. Astrophys. 530, A80.

Stewart, A., et al., in prep. LOFAR NCP Transient Search.

Sutherland, W., Saunders, W., Dec. 1992. On the likelihood ratio for source identification. Mon. Not. R. Astron. Soc. 259, 4130.

Swinbank, J., Jul. 2011. The LOFAR Transients Pipeline. In: Evans, I. N., Accomazzi, A., Mink, D. J., Rots, A. H. (Eds.), Astronomical Data Analysis Software and Systems XX. Vol. 442 of Astronomical Society of the Pacific Conference Series. p. 313.

Swinbank, J. D., 2014. Comet: A VOEvent broker. Astron. Comp. 7, 12–26.

Szalay, A., et al., 2006. Indexing the sphere with the Hierarchical Triangular Mesh. MSR TR 2005 123, The John Hopkins University, Microsoft Research and CERN.

Taylor, G. B., et al., Dec. 2012. First Light for the First Station of the Long Wavelength Array. Journal of Astronomical Instrumentation 1, 50004.

Thyagarajan, N., et al., Nov. 2011. Variable and Transient Radio Sources in the FIRST Survey. Astrophys. J. 742, 49.

Tingay, S. J., et al., Jan. 2013. The Murchison Widefield Array: The Square Kilometre Array Precursor at Low Radio Frequencies. Publ. Astron. Soc. Aus. 30, 7.

Usov, V. V., Katz, J. I., Dec. 2000. Low frequency radio pulses from gamma-ray bursts? Astron. Astrophys. 364, 655–659.

van der Laan, H., Sep. 1966. A Model for Variable Extragalactic Radio Sources. Nature 211, 1131.

van der Tol, S., Jeffs, B. D., van der Veen, A.-J., Sep. 2007. Self-Calibration for the LOFAR Radio Astronomical Array. IEEE Transactions on Signal Processing 55, 4497–4510.

van Haarlem, M. P., et al., Aug. 2013. LOFAR: The LOw-Frequency ARray. Astron. Astrophys. 556, A2.

Welch, J., et al., Aug. 2009. The Allen Telescope Array: The first widefield, panchromatic, snapshot radio camera for radio astronomy and SETI. IEEE Proceedings 97, 1438–1447.

Whitaker, J. C., 1996. The Electronics Handbook. CRC Press.

Williams, P. K. G., et al., Jan. 2013. ASGARD: A Large Survey for Slow Galactic Radio Transients. I. Overview and First Results. Astrophys. J. 762, 85.

Williams, R. D., Barthelmy, S. D., Denny, R. B., Graham, M. J., Swinbank, J., Sep. 2012. Responding to the Event Deluge. Vol. 8448 of SPIE Conf. Ser.

Wolter, K. M., 1984. An investigation of some estimators of variance for systematic sampling. Journal of the American Statistical Association 79 (388), 781–790.
URL http://www.jstor.org/stable/2288708